Applied Thermal Engineering 257 (2024) 124291

Contents lists available at ScienceDirect

Applied Thermal Engineering

journal homepage: www.elsevier.com/locate/apthermeng

Research Paper

Computational fluid dynamics simulation of cryogenic vertical upflow boiling under Earth gravity

Sunjae Kim [a], Jason Hartwig [b], Issam Mudawar [a,*]

[a] Purdue University Boiling and Two-Phase Flow Laboratory (PU-BTPFL), School of Mechanical Engineering, Purdue University, 585 Purdue Mall, West Lafayette, IN 47907, USA

[b] Fluids and Cryogenics Branch, NASA Glenn Research Center, 21000 Brookpark Rd, Cleveland, OH 44135, USA

ARTICLE INFO

Keywords:
Cryogenic flow boiling
Computational Fluid Dynamics
Two-phase flow
Space applications

ABSTRACT

This study presents numerical simulations and their validation for flow boiling of liquid nitrogen (LN_2) in a vertical upflow orientation, with a primary aim to understand the complex two-phase flow and heat transfer phenomena important to space applications. The computational fluid dynamics (CFD) model utilized the coupled level set volume of fluid (CLSVOF) method, incorporating additional source terms for bubble collision dispersion force and shear lift force in the momentum conservation equation to enhance simulation accuracy. The simulations were conducted for two mass velocities (G = 526 and 804 kg/m^{2}s) and three different heat flux levels (approximately 10%, 30%, and 70% of critical heat flux (CHF) under Earth gravity. The model was validated against measured wall temperature data acquired from the authors' previous experimental studies, demonstrating average deviations of less than 2.8 K across all operating conditions. The simulated two-phase flow contours illustrated various flow patterns, including bubbly, slug, churn, and annular. Both mass velocity and heat flux were observed to impact the onset of nucleate boiling (ONB), bubble nucleation, growth, and coalescence, and overall vapor structure. The simulations also offered insight into axial and radial void fraction and velocity profiles, revealing local flow acceleration trends synchronized with void fraction development. A comparison between predicted and measured bulk fluid temperature profiles showed excellent agreement, further validating the CFD model's accuracy and practical usefulness for two-phase cryogenic flow boiling simulations in space applications.

1. Introduction

1.1. Flow boiling physics and multiphase CFD simulations

In the contemporary era of space exploration, there is an escalating demand for improved predictability of a broad variety of applications involving the use of cryogens, from deployment of spacecraft and both commercial and military satellites to fuel depots and the establishment of extraterrestrial human habitats. Because of their low boiling points, cryogens in these applications exist mostly as two-phase vapor–liquid mixtures. Herein lies the difficulty in predicting the fluid physics and heat transfer behavior of cryogens, which is exasperated by their unique thermophysical properties compared to those of common room temperature fluids. Phase change is also encountered in a variety of thermal management systems that are used to tackle heat removal from electronic and power devices across various space missions. The operational demands in these missions and associated subsystems invariably lead to the generation of significant thermal loads, which can cause degradation of system performance, let alone the potential for serious system failures. In response, substantial research endeavors have been dedicated to the development and optimization of various two-phase thermal management systems, which are critical for safe and efficient dissipation of large thermal loads while maintaining the desired weight efficiency. Many thermal researchers and engineers, including those at the Purdue University Boiling and Two-Phase Flow Laboratory (PU-BTPFL) have developed high-performance two-phase cooling schemes, including hybrid-cooling [1,2], bidirectional counter-flow heat sinks [3] and manifold micro-channel heat sinks [4,5], let alone more conventional schemes: pool boiling [6,7], spray [8–10] and jet impingement [11,12], and mini/micro-channel heat sinks [13–16]. Currently, thermal management efforts are increasingly being focused on ability to greatly increase heat transfer coefficients using compact and lightweight architectures. The uniqueness of many of these thermal management

* Corresponding author.
E-mail address: mudawar@ecn.purdue.edu (I. Mudawar).

https://doi.org/10.1016/j.applthermaleng.2024.124291
Received 27 April 2024; Received in revised form 18 August 2024; Accepted 29 August 2024
Available online 31 August 2024

Nomenclature

c	cell size (mm)
C_D	bubble drag coefficient
C_L	coefficient in Eq. (19)
$c_{p,f}$	specific heat of liquid (J/kgK)
d	distance from local cell to interface (m)
D_b	bubble diameter (m)
d_b	average bubble diameter (m)
D_i	tube's inner diameter (mm)
D_o	tube's outer diameter (mm)
E	energy per unit mass (J/kg)
f	Fanning friction factor
F	force per cell volume (N/m^3)
F_{BCD}	volumetric bubble collision dispersion force (N/m^3)
F_{SLF}	shear lift force per unit volume (N/m^3)
F_{st}	surface tension force per unit volume (N/m^3)
G	mass velocity (kg/m^{2}s)
g	gravitational acceleration (m/s^2)
g_e	Earth gravity (m/s^2)
h	enthalpy (J/kg); heat transfer coefficient (W/m^{2}K)
h_{fg}	latent heat of vaporization (J/kg)
K	proportionality constant
k_{eff}	effective thermal conductivity (W/m•K)
L	total length of heated tube (m)
L_e	entrance length of heated tube (m)
L_H	heated length of heated tube (m)
L_{sp}	upstream single-phase liquid length of heated tube (m)
$\dot{m}$	mass flow rate (kg/m^3•s)
$\vec{n}$	interface normal vector
p	pressure (Pa)
q''	heat flux (W/m^2)
r	radial coordinate (m)
r_i	mass transfer intensity factor (1/s)
Re	Reynolds number
S_h	energy source by phase change (J/m^3)
T	temperature (°C, K)
t	time (s)
TC	thermocouple
Th	wall thickness (m)
u	velocity (m/s)
u_t	liquid fluctuation velocity due to bubble agitation (m/s)
u_τ	frictional velocity (m/s)
x_e	thermodynamic equilibrium quality
y	coordinate in computational domain perpendicular to tube wall (m)
y^+	dimensionless distance perpendicular to tube wall
Y_B	distance from wall to tip of vapor bubble (m)
z	axial coordinate in computational domain (m)

Greek symbols

α	void fraction
α_{max}	dense packing limit
ε	turbulent dissipation (m^2/s^3)
κ	curvature
μ	dynamic viscosity (kg/m•s)
ν	kinematic viscosity (m^2/s)
ρ	density (kg/m^3)
σ	surface tension (N/m)
τ	shear stress (N/m^2)
φ	level-set function

Subscripts

b	bubble
CHF	critical heat flux
cond	condensation
d	departure
e	equilibrium
evap	evaporation
f	liquid
fo	liquid-only
g	vapor
i	inner tube wall, interface
in	inlet to heated tube
meas	measured (experimental)
o	outer tube wall
out	outlet
pred	predicted
s	solid wall
sat	saturation
sc	subcooling
sp	single phase liquid
w	heated wall
z	local

Acronyms

AIAD	Algebraic Interfacial Area Density
BCD	Bubble Collision Dispersion
CFD	Computational Fluid Dynamics
CFM	cryogenic fluid management
CHF	critical heat flux
CLSVOF	Coupled Level-Set and Volume-of-Fluid method
CSF	Continuous Surface Force
DNS	Direct Numerical Simulation model
HTC	heat transfer coefficient
HV	hand (ball) valve
ISS	International Space Station
LBM	Lattice Boltzmann Model
LN_2	liquid nitrogen
LS	level-set
NTP	nuclear thermal propulsion
ONB	onset of nucleate boiling
PU-BTPFL	Purdue University Boiling and Two-Phase Flow Laboratory
PWR	pressurized water reactor
SST	Shear-Stress Transport
SV	solenoid valve
UDF	user-defined function
VOF	Volume-of-Fluid model

schemes demands extensive experimental efforts which are aimed at developing broad-based databases from which empirical correlations are developed for both two-phase pressure drop and heat transfer.

Concurrently, as summarized in Table 1, computational investigations of flow boiling have been actively pursued alongside experimental investigations. As categorized in Table 1, two-phase flow boiling computational studies can be grouped into three different categories: (a) studies utilizing a single fluid mixture model such as the Volume of Fluid (VOF) model without artificial nucleation cavities along the boiling surface, (b) studies employing the VOF model with artificial nucleation cavities, and (c) studies utilizing the Eulerian-Eulerian two-fluid model. The preference for studies employing the single fluid mixture model, exemplified by the widespread use of the VOF model over the two-fluid model, underscores the VOF model's efficacy as a

Table 1
Summary of recent flow boiling CFD studies with room temperature fluids.

Category	Authors	Year	Fluid	Interface tracking model	Phase change model	Artificial nucleation sites	Remarks
VOF without artificial cavities	Kim & Lee [17]	2019	water	VOF	Hardt & Wondra's model [18]	None	• Compared hydrophilic and hydrophobic microchannel flow boiling of water • Reported enhanced bubble nucleation on hydrophobic surface • Reported increased active nucleation site density on hydrophobic surface • Reported capability of "VOF+HW Model" combination at capturing effect of hydrophobicity on bubble nucleation dynamics
	Kim et al. [19]	2020	water	VOF	Lee model	None	• Studied effect of hydrophobic surface patterning on microchannel flow boiling of water • Reported enhanced bubble nucleation on dotted hydrophobic pattern surfaces • Reported significantly increased nucleation site density on hydrophobic pattern surfaces • Reported capability of "VOF+Lee Model" combination at capturing surface patterning effect on bubble nucleation dynamics
	Tang et al. [21]	2024	HFE-7100	VOF	Lee model	None	• Compared different geometries of microchannel in terms of thermal–hydraulic performance • Multiple flow regimes simulated for bubbly flow, slug flow, and vapor columns • Reported different pressure stability trends for each geometry
	Huang et al. [22]	2024	R1233zd (E)	VOF	Lee model	None	• Simulated parallel channel instability and validated results against experimental data • Reported capability of "VOF+Lee Model" combination at capturing instability mechanism in parallel microchannels: Flow oscillation – Reversed flow – Flush back
	Broughton et al. [23]	2024	HFE-7200	VOF	Lee model	None	• Compared flow boiling performance in two different microchannel geometries in terms of pressure drop and heat transfer coefficient • Reported different flow regimes simulated for each microchannel geometry
	Cui et al. [24]	2024	Water	VOF	Lee model	None	• Simulated flow boiling performance in microchannel with varying aspect ratio • Reported superior heat dissipation ability of high aspect ratio microchannel geometry
	Guo et al. [25]	2024	Water	VOF	Lee model	None	• Controlled and varied surface roughness using Fourier expressions • Reported enhanced bubble nucleation with higher and wider roughness geometry • Reported capability of "VOF+Lee Model" combination at capturing surface roughness effect on bubble nucleation dynamics
	Mudawar et al. [26]	2024	nPFH	CLSVOF	Lee model	None	• Simulated microgravity flow boiling and validated simulated wall temperature and flow contours against experimental data acquired from ISS experiments • Reported limited contribution of microlayer effect for macro-channel flow boiling • Reported capability of "VOF+Lee Model" combination at simulating reduced gravity flow boiling
VOF with artificial cavities	Sato and Niceno [27]	2017	Water	VOF	Sharp interface model	Multiple artificial nucleation sites	• Involved only heterogenous nucleation • Pre-designated nucleation sites on heated surface domain • Calculated activated nucleation sites based on empirical correlations of water pool boiling • Reported limitation of boiling model to correctly simulate heterogenous nucleation
	Chen et al. [28]	2022	Water	VOF	Sharp interface model	Multiple artificial nucleation sites	• Pre-designated nucleation sites on heated surface domain • Calculated activated nucleation sites based on empirical correlations for water pool boiling
	Chen et al. [29]	2023	Water	VOF	Sharp interface / Microlayer model	Multiple artificial nucleation sites	• Pre-designated nucleation sites on heated surface domain • Calculated activated nucleation sites based on empirical correlations for water pool boiling • Reported large deviation by using only artificial heterogenous nucleation model without microlayer evaporation model • Reported reduced effectiveness of artificial heterogenous nucleation when combined with microlayer evaporation model

(*continued on next page*)

Table 1 (*continued*)

Category	Authors	Year	Fluid	Interface tracking model	Phase change model	Artificial nucleation sites	Remarks
Others	Alimoradi et al. [30]	2021	Water	Two-fluid model	Wall boiling model	None	• Simulated surface roughness effect on flow boiling • Reported enhanced heat transfer efficiency with larger roughness • No simulated flow contours reported
	Mitrakos et al. [31]	2023	Water	Two-fluid model	Wall boiling model	None	• Simulated water flow boiling with different bubble departure diameter closure relations • Reported further refinements of closure relations are required

robust multiphase interface tracking model for flow boiling simulations. This is attributed to VOF model's ability to accurately capture detailed two-phase flow patterns and interfacial behavior. Supporting the assertion, a study by Kim et al. [19] investigated the impact of hydrophobic surface on the performance of microchannel flow boiling with water, using a combination of VOF model and the Lee model [20] for phase change. Their simulations demonstrated a marked increase in nucleation site density on hydrophobic surfaces, resulting in an enhancement of bubble nucleation. Furthermore, Guo et al. [25] devised a method to emulate surface roughness using Fourier functions and investigated the influence of surface roughness on flow boiling performance using water, again utilizing the VOF model in conjunction with the Lee model. Their simulation results showed that larger and wider roughness geometries resulted in enhanced bubble nucleation, highlighting the ability of the "*VOF+Lee model*" combination to accurately predict bubble nucleation dynamics in response to varying surface roughness conditions. Expanding on the conventional VOF model, Mudawar et al. [26] employed the Coupled Level Set Volume of Fluid (CLSVOF) method alongside additional momentum sources such as shear lift force, bubble collision dispersion force, and drag force to simulate microgravity flow boiling physics observed in the International Space Station (ISS), here too without incorporating artificial nucleation cavities. Their computation results were validated against wall temperature data and flow visualization data acquired from the ISS Flow Boiling and Condensation Experiment (FBCE). This validation confirmed the capability of the "*VOF+Lee model*" combination to accurately predict the influence of reduced gravity on flow boiling physics.

Meanwhile, there is another simulation approach that employs the VOF model with artificial nucleation cavities to simulate heterogeneous bubble nucleation. Sato and Niceno [27] randomly placed bubble nucleation sites on the heated surface which were activated based on an empirical correlation that calculated the number of active nucleation sites corresponding to prescribed wall superheat. However, the authors noted that the empirical correlation is validated only for water and may not be applicable to other fluids. They suggested potential future improvements could be pursued by employing a more detailed mechanistic boiling model instead of empirical correlations to reliably simulate the effect of surface imperfections on bubble nucleation dynamics. Similarly, Chen et al. [28] simulated water flow boiling in microchannels using the VOF model with artificial nucleation sites. They employed empirical correlations for nucleation site density which are developed based on water pool boiling, to calculate the number of activated nucleation sites corresponding to 3, 5, and 10 K wall superheats. Like the study by Sato and Niceno [27], the empirical correlation used in Chen et al. [28] is applicable only to water and not for flow boiling with other fluids. Additionally, a subsequent study by Chen et al. [29] reported the potential enhancement of the artificial heterogeneous nucleation scheme through the incorporation of a microlayer evaporation model, albeit limited to water flow boiling.

Recognizing the limitations of the artificial nucleation approach due to the lack of reliable empirical correlations or mechanistic models for fluids other than water, the combination of "*VOF+Lee model*" emerges as a preferable option for flow boiling simulations with fluids like cryogens, offering several advantages over other models: (1) ability to accurately capture interfacial behavior and two-phase flow patterns and regime transitions, (2) ability to accurately predict trends in bubble nucleation for different surface conditions as validated by previous studies, and (3) relatively economical computational cost compared to other numerical models like Lattice Boltzmann Model (LBM) or Direct Numerical Simulation (DNS) model.

1.2. Recent cryogenic CFD studies and their potential application to future cryogenic space systems

Capitalizing on the benefits afforded by the combination of the VOF model and Lee model, numerous CFD studies have been carried out for various cryogenic two-phase systems, as summarized in Table 2. For instance, Wang et al. [32] conducted film boiling simulations for four different cryogenic fluids under constant temperature boundary conditions applied to the heated surface and demonstrated the temporal evolution of flow regimes. They also systematically investigated the effect of heater size on bubble diameter by varying the size of the heated surface and identified the relationship between bubble diameter and the "most dangerous" Taylor wavelength. Xu et al. [34] employed "*VOF+Lee model*" in their simulations to investigate the heat exchange process within a spiral heat exchanger, using LNG as the working fluid. They reported an average deviation of 30 % between the predicted and the measured pressure drops. This finding underscores the capability of "*VOF+Lee model*" to predict pressure drop in cryogenic systems. Indeed, research efforts have extended beyond terrestrial ground-based applications to encompass cryogenic space applications as well. Jiang et al. [35] employed "*VOF+Lee model*" to simulate the boil-off rate of LH_2 in cryogenic tank storage. Their simulations, conducted under varying reduced gravity levels (10^{-2} – $10^{-5}g_e$), demonstrated the pronounced effects of convection and buoyancy under higher gravity conditions, which increased heat transfer efficiency and ultimately led to a faster boil-off rate with increasing gravity.

Several researchers [35–37] utilized the Eulerian-Eulerian two-fluid model, in conjunction with a phase change model called the wall boiling model, to simulate the transfer of cryogenic liquid propellant from tank to tank or from tank to space vehicle. The wall boiling model requires segregation of the wall heat flux into different components, such as quenching heat flux, convective heat flux, and latent heat flux. Calculating these components necessitates utilization of bubble dynamic parameters, including bubble departure diameter, bubble departure frequency, and nucleation site density. However, as previously mentioned, this information has not been reported or correlated for cryogenic fluids yet, rendering accurate numerical simulation using the Eulerian-Eulerian two-fluid model challenging. Recently, Ajuha et al. [40] employed empirical correlations for bubble nucleation parameters for water, which they scaled for liquid nitrogen. They then conducted line chilldown simulations and validated their scaling factors based on cryogenic chilldown experimental data. Overall, a major drawback of the two-fluid model is its inability to capture sharp interface morphology, rendering it incapable of accurately simulating two-phase flow patterns during flow boiling. Thus far, none of the studies utilizing two-fluid models have reported reliable flow contour predictions, two-phase flow patterns, or transitions between patterns.

Table 2
Summary of recent CFD studies with cryogenic fluids.

Category	Authors	Year	Fluid	Simulated System	Interface tracking model	Phase change model	Remarks
VOF based model	Wang et al. [32]	2022	LH_2 LO_2 LN_2 LCH_4	Film boiling	VOF	Lee model ($r_{i,evap} = 1000$)	• Constant surface temperature boundary conditions • Reported temporal evolution of flow regimes • Reported effect of heater size based on most dangerous Taylor wavelength • Reported effect of reduced gravity simulated but not validated
	Kim et al. [48]	2023	LN_2	Flow boiling	CLSVOF	Lee model ($r_{i,evap} = 1000$)	• Enhanced simulation accuracy by applying additional momentum source called bubble collision dispersion force • Simulated LN2 flow boiling in a vertical upflow cylindrical channel • Reported developing two-phase flow regimes under different heat fluxes • Reported capability of "CLSVOF+Lee model" combination at predicting cryogenic flow boiling heat transfer physics
	Huo et al. [33]	2023	LHe	Oscillating heat pipe	VOF	Lee model ($r_{i,evap} = 20$)	• Reported temporal flow regime development in heat pipe • Reported capability of "VOF+Lee model" combination at simultaneously capturing both cryogenic evaporation and condensation
	Xu et al. [34]	2023	LNG	Spiral heat exchanger	VOF	Lee model ($r_{i,evap} = 3$)	• Simulated pressure drop for cryogenic LNG heat exchanger • Average deviation of 30 % against experiment data • Reported capability of "VOF+Lee model" combination at predicting cryogenic pressure drop
	Jiang et al. [35]	2023	LH_2	Cryogenic tank storage	VOF	Lee model ($r_{i,evap} = 0.1$)	• Simulated hydrogen boil-off rate under varying reduced gravity accelerations ($10^{-2} - 10^{-5} g_e$) • Reported more pronounced convection flow and heat transfer under higher gravity conditions • Reported faster boil-off rate under higher gravity conditions
	Hong et al. [36]	2023	LHe	Superconducting magnet cooling	VOF	Non equilibrium model	• Simulate helium bubble accumulation issues under high electromagnetic force field • Predicted reduced bubble accumulation with highly subcooled LHe
Non-VOF based model	Chen et al. [37]	2018	LN_2	Line chilldown	AIAD	Wall boiling model	• Did not provide reliable closure relations for cryogens (bubble diameter, departure frequency, nucleation site density)
	Zheng et al. [38]	2020	LH_2	Flow boiling	Two-fluid model	Wall boiling model	• Did not report cryogenic interfacial structure • Did not provide reliable closure relations for cryogens (bubble diameter, departure frequency, nucleation site density)
	Gubaidullin and Snigerev [39]	2020	LN_2	Flow boiling	Two-fluid model	Wall boiling model	• Did not report cryogenic interfacial structure • Did not provide reliable closure relations for cryogens (bubble diameter, departure frequency, nucleation site density)
	Ajuha et al. [40]	2024	LN_2	Line chilldown	Mixture model	Wall boiling model	• Did not provide reliable closure relations for cryogens (bubble diameter, departure frequency, nucleation site density) • Scaled existing closure relations to simulate cryogens

Therefore, to ensure reliable and useful CFD predictions for cryogenic flow boiling, it is imperative to apply the combination of the "*VOF+Lee model*". This approach not only enables the generation of precise forecasts for thermal–hydraulic parameters but also facilitates the simulation of cryogenic two-phase flow regimes and their transitions along a heated tube. Consequently, this modeling approach allows for a comprehensive understanding of the crosslink between two-phase heat transfer performance of cryogens and two-phase flow structures and interface behaviors.

1.3. Objectives of present study

The present study investigates the performance of 2-D axisymmetric computational fluid dynamics (CFD) in prediction of boiling characteristics of liquid nitrogen (LN_2) flowing vertically upwards along a uniformly heated circular tube. As clarified in the previous sections, the combination of the "*VOF+Lee model*" demonstrates substantial benefits in simulating two-phase flow boiling physics. However, due to the inherent limitations of the single mixture model, the VOF model underrepresents phase interactions exerted by phase velocities [26]. To address these limitations, this study introduces an advanced interface tracking method called CLSVOF, along with additional momentum sources of shear lift force and bubble collision dispersion force, to further enhance the accuracy of the cryogenic flow boiling simulations.

The primary objective of this study is to evaluate and demonstrate the capabilities of the proposed CFD model using CLSVOF and additional momentum terms as a reliable design tool for cryogenic flow boiling systems. To establish the reliability of the CFD model, the obtained results are rigorously validated against heat transfer measurements acquired from recent cryogenic experiments conducted by the present authors [43]. Subsequently, to demonstrate added usefulness of the CFD simulations, the validated CFD model is employed to predict the fluid flow and heat transfer characteristics for selected operating conditions under $1g_e$ Earth gravity which are otherwise very difficult to measure in cryogenic experiments. This encompasses axial variations of interfacial two-phase flow patterns, as well as axial and radial distributions of void fraction, fluid velocity, and fluid temperature. Therefore, the results of this numerical study will serve as a steppingstone, enhancing both the reliability and usefulness of the proposed CFD model as alternative design tools for future cryogenic space applications employing two-phase flow boiling.

2. Experimental methods

2.1. Experiment facility

The present study utilizes cryogenic flow boiling data derived from recent experimental investigations conducted by the present authors. Therefore, only a brief overview of the experimental methods is discussed herein to facilitate comprehension of the obtained outcomes. For further details on the different components, instrumentation, measurement uncertainties, operating procedure, imaging technique, and more, the reader is encouraged to consult the original publications where these experiments were initially documented. This includes 1-g_e horizontal LN_2 flow boiling experiments [41], microgravity LN_2 flow boiling experiments conducted aboard parabolic flight aircraft [42], and 1-g_e multiple flow orientation LN_2 flow boiling experiments [43], covering vertical upward, vertical downward, 45° inclined upward, and 45° inclined downward orientations. Note that maximum uncertainties in instrumentation measurements of measured parameters are given in Table 3.

Within the present database, the majority of cases exhibited uncertainty in $h_{tp,z}$ that remained below 10 %, as visually represented in Fig. 7 (a).

2.1.1. Two-phase flow loop

Fig. 1 depicts a schematic of the open-loop two-phase flow system utilized to (i) provide working fluid, LN_2, into the test section, and (ii) safely vent fluid from the test section outlet to ambient air. Since the loop is designed as an open circuit, a nitrogen gas cylinder is connected to the LN_2 dewar to provide positive ullage pressure and displace the LN_2 from the dewar. A turbine flow meter is employed to measure the volume flow rate of the liquid. For accurate determination of the mass flow rate, fluid density information is necessary. To obtain precise thermophysical property values for the incoming liquid, the temperature and pressure of the fluid are measured immediately downstream from the flow meter. The liquid then enters the test section, where a finite amount of heat is added, causing the fluid to undergo phase change and emerge as a two-phase mixture. At the outlet of the test section, fluid temperature and pressure are measured at the same axial location. The fluid is then directed into an adiabatic visualization chamber utilizing a transparent Pyrex tube, which permits interfacial behavior to be captured with the aid of a high-speed video camera (additional design details relating to the test section and visualization chamber are provided in the next section). To regulate the flow rate, a cryogenic grade needle valve is installed downstream of the visualization section. Two 3-kW rated vent heaters are serially connected downstream of the needle valve to completely evaporate any remaining two-phase mixture to pure vapor phase. At the outlet of the second vent heater, fluid temperature and pressure are measured. Farther downstream, the flowline is connected to a receiver tank which serves to eliminate any possibility of liquid escaping outboard in improbable situations such as vent heater power loss. Finally, the vapor is safely discharged through a vent hose to the ambient environment.

2.1.2. Heat transfer test section and visualization section

The primary components of the experimental facility are the test section and the visualization section. The test section is comprised of a heated tube that is enclosed within a vacuum chamber serving to minimize heat loss. As shown in Fig. 2, the vacuum chamber has an inner diameter (i.d.) of 100 mm and length of 800 mm, and is fitted with flanges on both ends to ensure vacuum tight enclosure. A center hole is machined through each flange for insertion of the heated test section. The vacuum chamber is equipped with four feedthrough ports. Two feedthroughs near to the outlet are for vacuum hose connections while the foremost feedthrough passes wires from the thermocouples attached to the outer wall of the heated tube to an external control box containing the data logger. The fourth feedthrough passes heater power leads from the test section's eight heaters. The heated test section assembly is comprised of the heating tube, eight individual heaters, and thermocouples wires. The heated tube is a thin walled ($Th = 0.5$ mm) stainless steel (SS304) tube with i.d. of $D_i = 8.5$ mm, entrance length $L_e = 112$ mm, and heated length L_H=680 mm. Eight individual electrically powered coil heaters, depicted schematically in Fig. 2, surround the heated tube to provide uniform heat flux along the tube wall. At 120 VAC power input, each heater can dissipate up to 400 W, for a total capacity for the eight heaters of up to 3200 W. Seven diametrically opposite pairs of thermocouples are attached to the heated tube wall at seven axial locations. Detailed axial locations of the thermocouples are provided in table form in Fig. 2. Aside from using vacuum to minimize heat loss, the entire test section assembly is wrapped with layers of insulation which are covered with aluminum sheet to minimize loss by radiation.

Table 3
Measurement uncertainties.

Parameter	Maximum Uncertainty
Fluid temperature, T_f	± 0.5℃
Wall temperature, T_w	± 0.5℃
Volume flow rate, $\dot{V}$	± 0.1 % reading
Absolute Pressure, P	± 0.25 % reading
Heat input, Q	± 0.25 % reading

2.2. Data processing

Steady state data are extracted from recorded temporal data by identifying each heater increment and confirming wall temperature reaching steady state. Extracted temporal data are averaged for each steady state period. Necessary thermophysical properties for nitrogen are retrieved from NIST-REFPROP [44].

The nitrogen enters the test section as subcooled liquid. Test section inlet enthalpy is found based on measured inlet temperature, T_{in}, and inlet and pressure, P_{in}, as

$$h_{in} = h(T_{in}, P_{in}) \tag{1}$$

Test section local enthalpy, h, at any z location from the heated inlet, and outlet enthalpy, h_{out}, are both calculated by application of energy conservation,

$$h(z) = h_{in} + \frac{q''\pi D_i z}{G\left(\pi D_i^2/4\right)} \tag{2a}$$

$$h_{out} = h_{in} + \frac{q''\pi D_i L_H}{G\left(\pi D_i^2/4\right)} \tag{2b}$$

Local thermodynamic equilibrium quality, $x_{e,z}$, is calculated according to the relation

$$x_e(z) = \frac{h - h_f\big|_P}{h_{fg}\big|_P} \tag{3}$$

where h_f and h_{fg} are, respectively, the saturated liquid enthalpy, and the latent heat of vaporization corresponding to local pressure which is linearly interpolated between measured inlet pressure, P_{in} and outlet pressure, P_{out}.

Local fluid temperature is determined based on the following relations:

$$T_{f,z} = \begin{cases} T_{in} + \left(T_{sat}\big|_{xe=0} - T_{in}\right)\dfrac{Z}{L_{sp}} & x_{e,z} < 0 \\ T_{sat,z} & 0 \le x_{e,z} \le 1 \end{cases} \tag{4}$$

where L_{sp} is the heated single-phase length, which is calculated as

$$L_{sp} = \frac{G\left(\pi D_i^2/4\right)}{q''\pi D_i}\left(h_f\big|_{P_{in}} - h_{in}\right) \tag{5}$$

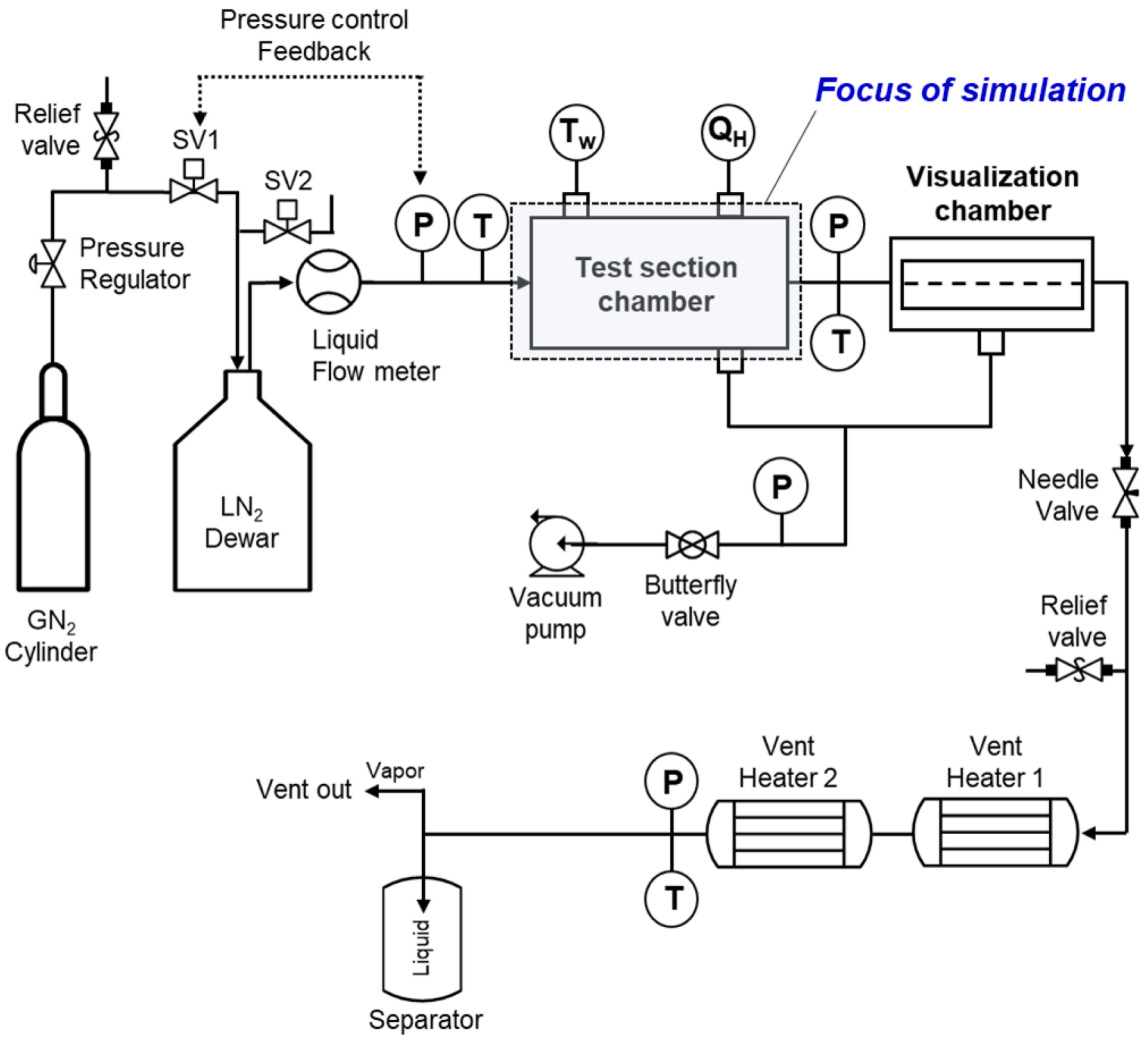

Fig. 1. Schematic of two-phase flow loop.

The local heat transfer coefficient (HTC) is defined based on measured local wall temperature and calculated local fluid temperature for each axial location,

$$h(z) = \frac{q''}{(T_{w,z} - T_{f,z})} \tag{6}$$

Local inner wall temperature, $T_{w,z}$, at each axial thermocouple location is determined from measured outer wall temperature, $T_{w,o,z}$, and measured heat flux, q", by accounting for conduction resistance across the heated tube wall,

$$T_w(z) = T_{w,o}(z) - \frac{q'' \pi D_i \ln(D_o/D_i)}{2\pi k_s} \tag{7}$$

3. Computational method

3.1. Computational sub-models and governing equations

This study employs transient analysis in ANSYS-Fluent to investigate flow boiling in a uniformly heated tube, under terrestrial Earth gravity and low inlet subcooling conditions. The dynamic behavior of two-phase fluid flow and heat transfer both across and along the heated length is tracked through transient analysis. To capture detailed interfacial structure, interface tracking is incorporated by means of the *Lee mass transfer* model [39] and *Continuous Surface Force* (CSF) model [45] with the transient CLSVOF method [46]. Additionally, the *Geo-Reconstruction scheme*, also known as the piecewise-linear method, and *anti-diffusion treatment* [47] are employed, respectively, to achieve sharp interface morphology and prevent false interfacial distortion induced by numerical diffusion. The *Shear-Stress Transport* (SST) *k-ω* turbulence model, which also accounts for viscous heating, is used to account for turbulence and eddy dissipation effects.

Despite the widespread use of VOF for two-phase simulations, interfacial forces governed by relative motion between phases are not accurately accounted for because of using a single momentum equation for both liquid and vapor phases. To improve the predictive capability of single momentum equation CFD models, it is crucial to incorporate additional momentum source terms that are not captured by the shared velocity and pressure fields [26]. To compensate for the inherent limitations of the VOF method, the present CLSVOF simulations incorporate additional important force terms, including (i) *shear-lift* and (ii) *bubble collision dispersion*.

Over the past six years, the described numerical model has undergone extensive validation for its adaptability to flow boiling simulations with cryogenic fluid [48], such as liquid nitrogen, and also with dielectric fluids, such as FC-72 or nPFH (n-perfluorohexane, C6F14) [26,49,51] under various gravitational acceleration conditions ranging from terrestrial Earth gravity down to microgravity.

Representatively, in 2019, an approach utilizing additional momentum sources has been proposed and applied to incorporate shear lift force for FC-72 flow boiling in a double-sided rectangular channel, simulating the Flow Boiling and Condensation Experiment (FBCE) [49].

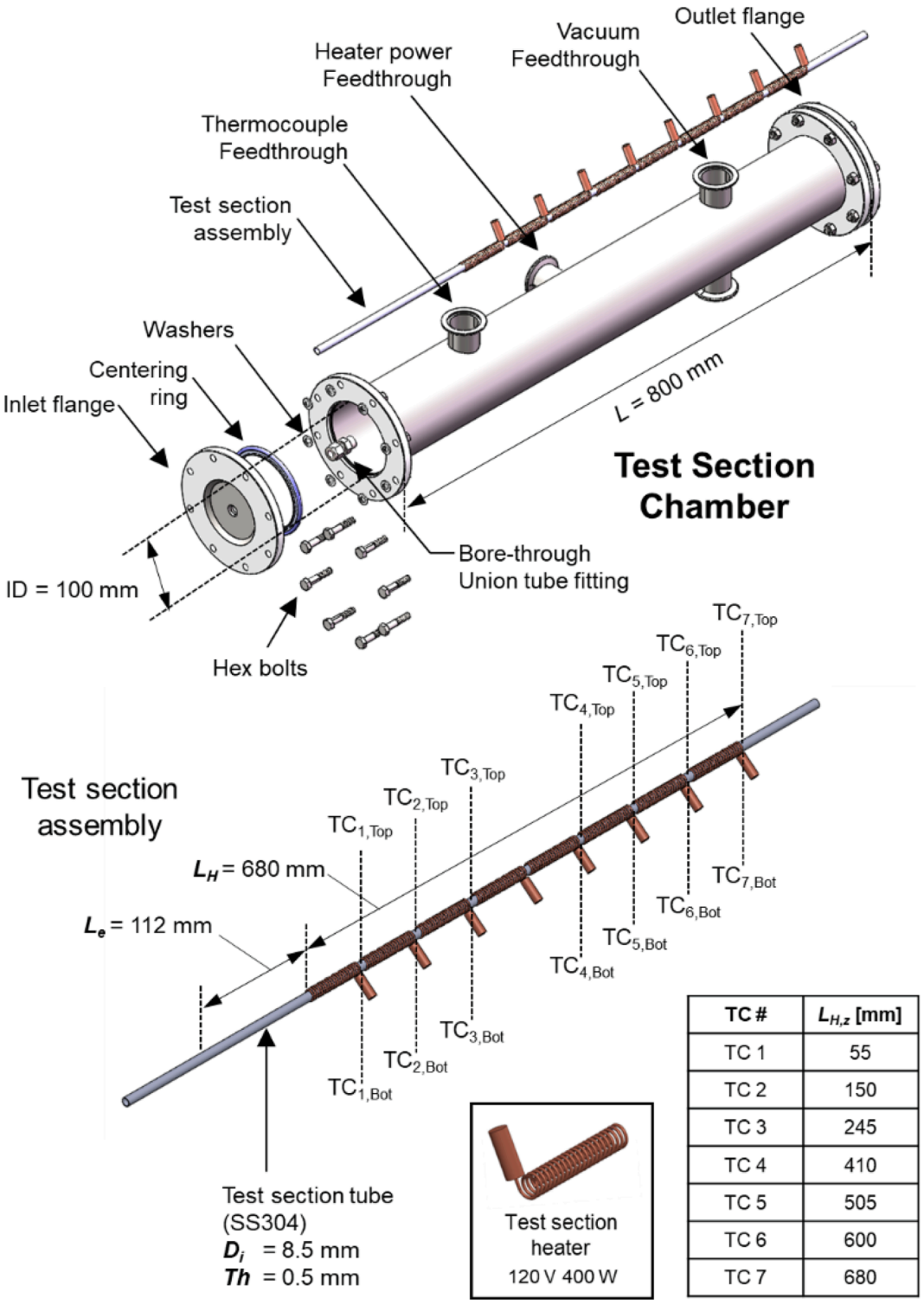

TC #	$L_{H,z}$ [mm]
TC 1	55
TC 2	150
TC 3	245
TC 4	410
TC 5	505
TC 6	600
TC 7	680

Fig. 2. Schematics of test section chamber and assembly.

In this study, the effect of shear lift force was validated by comparing simulation results with and without the shear lift force. The analysis clearly demonstrated the efficacy of the shear lift force on flow boiling simulation. In 2023, another momentum source term, the bubble collision dispersion force, was developed and implemented into the CFD model to simulate cryogenic flow boiling using liquid nitrogen [48]. The effect of the bubble collision dispersion force was analyzed in detail, demonstrating different simulation results with and without the additional momentum source term. The model's adaptability was validated against measured wall temperature and outlet void fraction from a benchmark liquid nitrogen flow boiling experiment of Lewis et al. [50]. Also in 2023, an advanced CFD model incorporating both shear lift force and bubble collision dispersion force was developed and utilized to simulate horizontal flow boiling of nPFH within a rectangular single-sided heating channel under terrestrial Earth gravity [51]. Predicted wall temperature and two-phase flow contours acquired from the model were compared to experimental data, validating the model's accuracy and efficacy. This study reported advanced two-phase flow contour

prediction performance when both shear lift force and bubble collision dispersion force were applied. Most recently, in 2024, the CFD model using both shear lift force and bubble collision dispersion force was adapted to simulate a flow boiling experiment onboard the ISS, validating the model's applicability for long-duration microgravity flow boiling using nPFH [26]. The CFD model utilized in this particular study is identical to the current CFD model employing CLSVOF along with both shear lift force and bubble collision dispersion force.

Likewise, from 2019 to 2024, extensive validation and demonstrations have proved the efficacy of the current CFD model for accurately predicting flow boiling physics. However, as mentioned in the introduction, the new model has not yet been tested for cryogenic flow boiling. Therefore, to fill the technological gap, the present study conducted simulations for liquid nitrogen flow boiling under terrestrial gravity conditions and validated the effectiveness of the current CFD model for cryogenic flow boiling simulations. Further details on governing equations and physics of the models are discussed in the following sections.

3.2. Governing equations

As indicated in Eqs. (8) and (9) below, mass conservation for each phase is expressed in terms of temporal variation and advection of corresponding volume fraction for each phase balanced by net mass transfer in and out of each cell via phase change,

$$\frac{\partial \alpha_f}{\partial t} + \nabla \bullet \left(\alpha_f \vec{u_f}\right) = \frac{1}{\rho_f} \sum \left(\dot{m}_{gf} - \dot{m}_{fg}\right) \tag{8}$$

$$\frac{\partial \alpha_g}{\partial t} + \nabla \bullet \left(\alpha_g \vec{u_g}\right) = \frac{1}{\rho_g} \sum \left(\dot{m}_{fg} - \dot{m}_{gf}\right) \tag{9}$$

where α, $\vec{u}$, $\dot{m}$, and ρ are volume fraction, velocity, mass flow rate per cell volume, and density, respectively, and subscripts f and g represent liquid and vapor, respectively.

The most distinctive feature of CLSVOF is inclusion of surface tension force in the momentum equation. Like VOF, CLSVOF involves solving a single mixture momentum equation using pseudo-mixture properties,

$$\frac{\partial (\rho \vec{u})}{\partial t} + \nabla \bullet (\rho \vec{u} \vec{u}) = -\nabla p + \nabla \bullet \mu \left[\nabla \vec{u} + (\vec{u})^T\right] - \sigma \kappa \delta(\varphi) \nabla \varphi + \rho \vec{g} + \sum F \tag{10}$$

where σ, κ, φ are surface tension, interface curvature, and level set function, respectively. Details concerning fluid property formulations are identical to those in VOF, which are available from ANSYS [52] and therefore, for purpose of brevity, will not be explained in this paper.

Energy conservation in CLSVOF model is identical to that in VOF and is given by

$$\frac{\partial (\rho E)}{\partial t} + \nabla \bullet (\vec{u}(\rho E + p)) = -\nabla \bullet \left(k_{eff} \nabla T\right) + S_h \tag{11}$$

where S_h is an energy source term describing latent heat transfer via phase change,

$$S_h = \dot{m}_{fg} h_{fg} \tag{12}$$

Interfacial mass transfer is modeled according to the Lee model [39],

$$\begin{cases} \dot{m}_{fg} = r_{i,evap} \alpha_f \rho_f \dfrac{(T_f - T_{sat})}{T_{sat}} & for evaporation \\ \dot{m}_{gf} = r_{i,cond} \alpha_g \rho_g \dfrac{(T_{sat} - T_g)}{T_{sat}} & for condensation \end{cases} \tag{13}$$

wherein $r_{i,evap}$ and $r_{i,cond}$ are empirical *mass transfer intensity factors* having unit of 1/s. It is widely known that values for these factors must be tailored to specifics of flow configuration, geometry, mesh, and even time step size. In general, excessively high values can pose numerical convergence issues, whereas very small values can result in appreciable discrepancy between interfacial and saturation temperatures. Based on the rigorous investigation of r_i values for cryogenic flow boiling from the authors' previous CFD study [48], r_i values of $r_{i,evap} = 1000$ and $r_{i,cond} = 100$ are used in this paper.

It must be noted that, unlike VOF, when using CLSVOF within ANSYS FLUENT, interfacial mass transfer terms in the mass and energy conservation equations are computed via user-defined functions (UDFs) as source terms for each phase.

3.3. Interface topography representation using CLSVOF

Ability of CLSVOF to provide more accurate interface topology than VOF is key to accurate simulation of surface tension force which, in turn, enhances accuracy in predicting overall force balance on individual bubbles and therefore more accurate prediction of the bubble formation cycle from nucleation to detachment.

As indicated in Eq. (10), the *level set function*, φ, used in CLSVOF is defined as a signed distance d to the interface, positive for primary (liquid) phase and negative for secondary (vapor) phase, with the interface designated as $\varphi = 0$.

$$\varphi(x,t) = \begin{cases} +|d| & if\ x\ belongs\ to\ primary\ phase \\ 0 & if\ x\ belongs\ to\ interface \\ -|d| & if\ x\ belongs\ to\ secondary\ phase \end{cases} \tag{14}$$

This formulation renders the level set function both smooth and continuous across the interface. In CLSVOF, interface normal vector, $\vec{n}$, and curvature, κ, are calculated, respectively, according to

$$\vec{n} = \left.\frac{\nabla \varphi}{|\nabla \varphi|}\right|_{\varphi=0} \tag{15}$$

$$\kappa = \nabla \bullet \left.\frac{\nabla \varphi}{|\nabla \varphi|}\right|_{\varphi=0} \tag{16}$$

This formulation represents a fundamental advantage over VOF, where the calculation of interface normal vector and curvature relies on spatial derivative of volume fraction, which is intrinsically discontinuous across the interface, resulting in compromised representation of the interface [48]. With reliance on the smooth and continuous level set function across the interface, CLSVOF enables accurate calculation of surface tension force and therefore more accurate capture and simulation of small bubble dynamics, fluid motion, and heat transfer.

3.4. Additional momentum source terms

3.4.1. Surface tension

Surface tension effects at interfaces are modeled by incorporating an addition force term F_{st} which is calculated using the *Continuum Surface Force* (CSF) model proposed by Brackbill et al. [45],

$$F_{st} = \sigma \frac{\rho \kappa \delta(\varphi)}{0.5(\rho_f + \rho_g)} \tag{17}$$

where F_{st} is the volumetric surface tension force and function $\delta(\varphi)$ is given by

$$\delta(\varphi) = \begin{cases} \dfrac{1 + \cos\left(\dfrac{\pi \varphi}{a}\right)}{2a} & if\ \ |\varphi| < 0 \\ 0 & if\ \ |\varphi| \geq 0 \end{cases} \tag{18}$$

wherein $a = 1.5\ h$, h being the grid spacing of local mesh.

3.4.2. Shear-lift force

To improve the prediction of near-wall bubble behavior and thus heat transfer, the shear-lift force formulation by Mei and Klausner [53]

is employed as a source term in the momentum equation using a UDF in ANSYS-Fluent. A correlation was developed using data for a wide range of Reynolds numbers and is given as

$$F_{SLF} = \frac{1}{8}\pi C_L \rho_f u_r^2 d_b^2 \tag{19}$$

where

$$C_L = 3.877 G_s^{1/2} \times \left[Re_b^{-m/2} + \left(0.344 G_s^{1/2}\right)^m \right]^{1/m}, m = 4 \tag{20}$$

and

$$G_s = \frac{1}{2}\left|\frac{du_r}{dy}\right| \frac{d_b}{u_r} \tag{21}$$

In the equations above, G_s is the dimensionless shear rate based on relative velocity u_r ($=u_f - u_g$) between the vapor bubble and liquid, d_b is the bubble diameter, and Re_b is the bubble Reynolds number based on bubble diameter as characteristic length.

3.4.3. Bubble collision dispersion force

As discussed in the Introduction, relative interfacial motion generated by different phase velocities is under-represented in single-equation models, including both VOF and CLSVOF. To correct this shortcoming and improve the present CLSVOF model's ability to more accurately predict bubble growth and detachment, which are both kernel for flow boiling simulations, an additional term which accounts for *Bubble Collision Dispersion (BCD) force* is included in the momentum

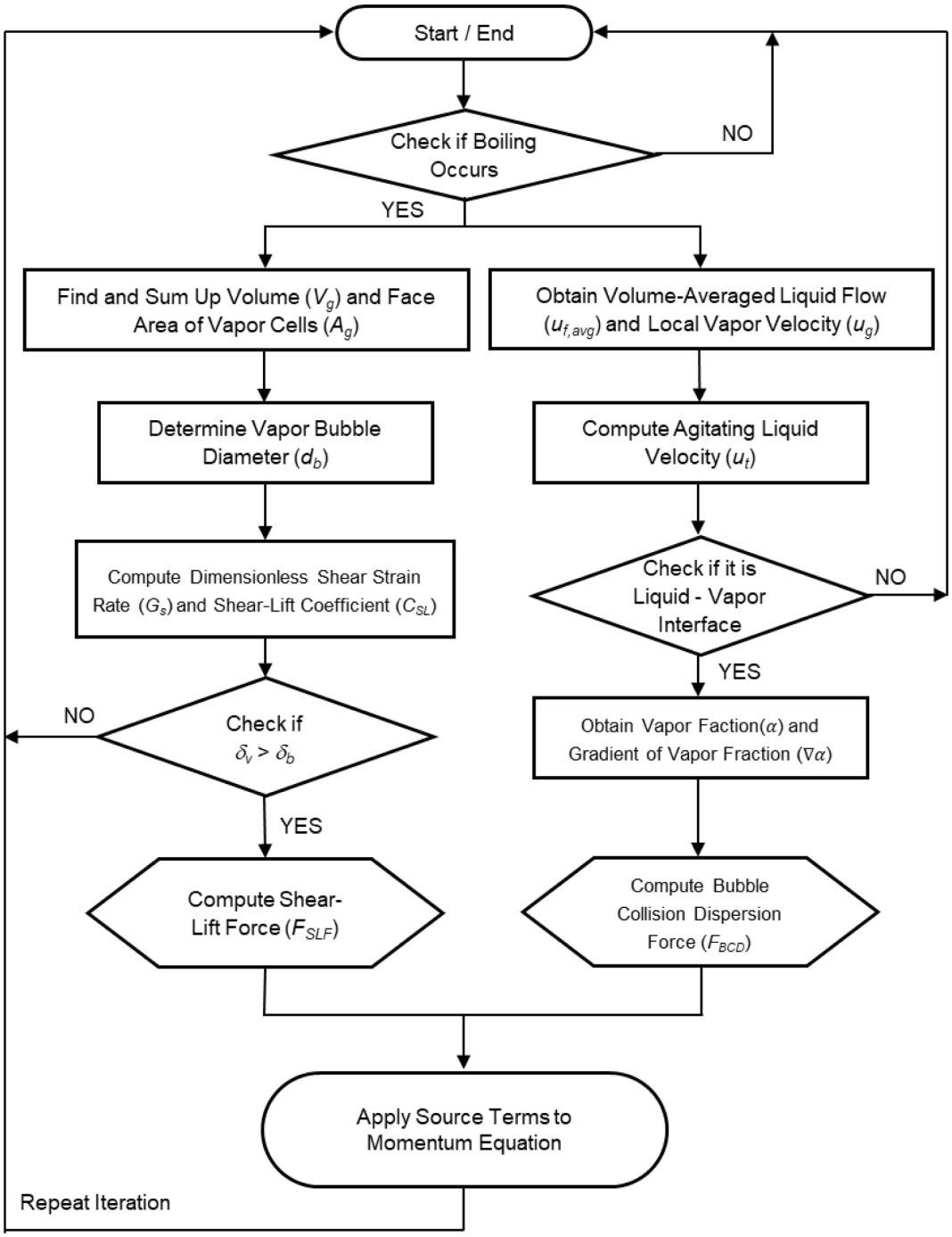

Fig. 3. Flow chart for the model computations, including effects of all the interfacial forces.

conservation equation as a source term. Sharma et al. [54] introduced the following relation for BCD force per unit volume of mixture,

$$F^{BCD} = -\left(K\frac{\rho_f u_t^2}{2\alpha_{g,max}^{2/3}}\right)f(\alpha_g)\nabla\alpha \tag{22}$$

where α_{max} and K are *dense packing limit* and proportionality constant, with recommended values for bubbly flow of 0.62 and 1, respectively, and α_g is void fraction. Also included in Eq. (13) are liquid fluctuation velocity, u_t, resulting from liquid agitation, which accounts for turbulent intensity effects on bubble dispersion, and function $f(\alpha_g)$, defined as

$$f(\alpha_g) = \alpha_g^{2/3}\left[1-\left(\frac{\alpha_g}{\alpha_{g,max}}\right)\right] \tag{23}$$

The liquid fluctuating velocity, u_t, in Eq. (22) is determined by net velocity difference between vapor phase velocity at each cell and average velocity of liquid flow, which is updated every iteration.

$$u_t = (\varepsilon D_b)^{1/3} \approx |\overline{u} - u_{local}| \tag{24}$$

More details on the effect of this force on flow boiling are described in the author's prior study [48].

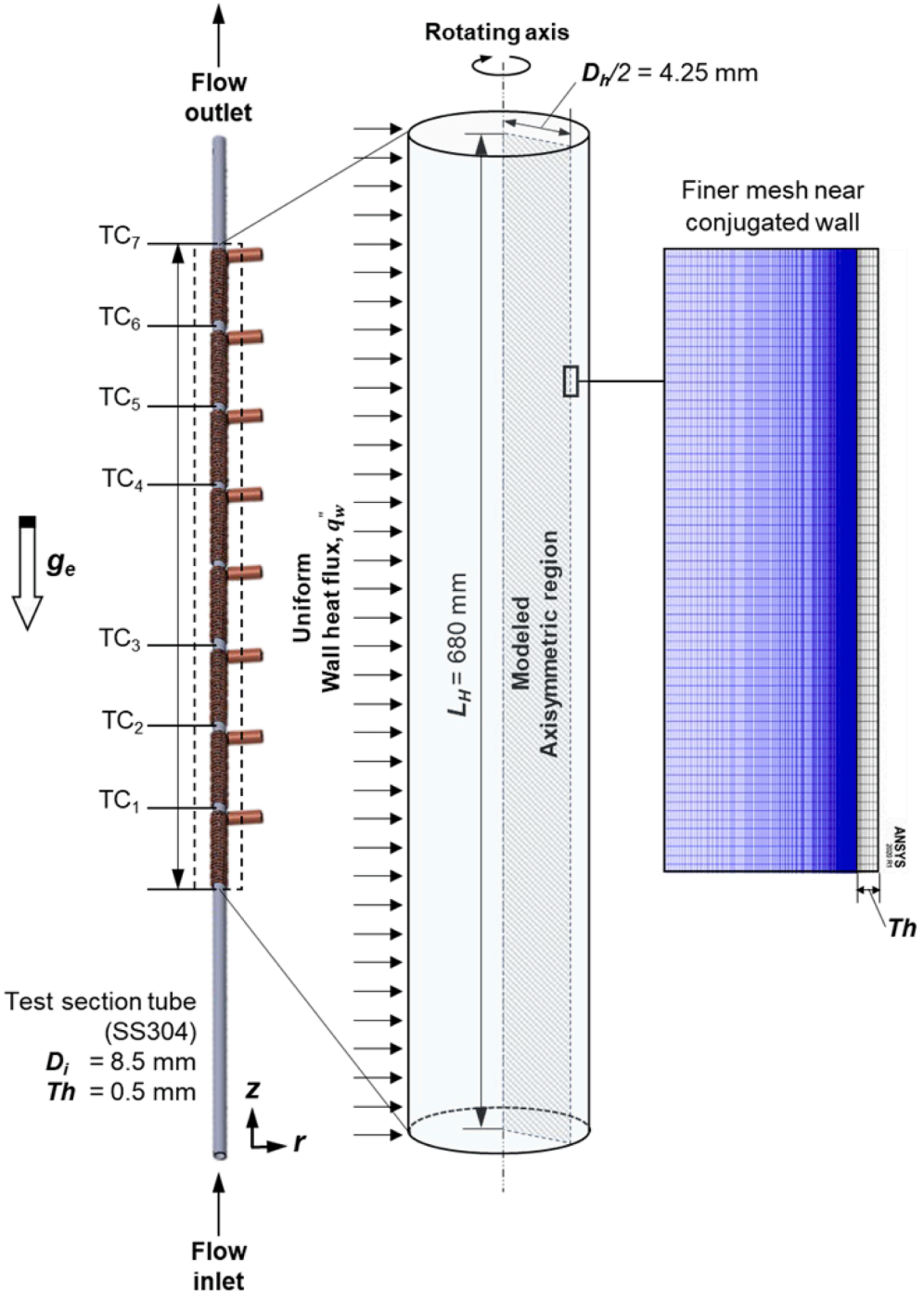

Fig. 4. Schematics of axisymmetric computational domain and mesh grid.

3.5. User-Defined function (UDF) adaptation

The UDF adopted in the present simulations is detailed in the flowchart depicted in Fig. 3. As the fluid enters the test section in subcooled liquid state, shear lift force plays no role at the beginning. Once phase change occurs, the algorithm identifies cells occupied by the vapor phase whose volume fraction is greater than or equal to a specific reference value of 0.5 and obtains total vapor volume within the entire domain through the summation of cells with vapor. It also sums all face areas where vapor contacts the thermally conjugated surface between the fluid and solid cells. These two values are saved into allocated memory, recalled by the UDF, and used to calculate the mean diameter of vapor every numerical iteration by dividing the total volume of vapor cells by the total surface area of vapor.

The detailed procedure for calculating the bubble collision dispersion force in the UDF is also described in the flowchart shown in Fig. 3. Since the fluid enters the test section in subcooled liquid state, the bubble collision dispersion force is nonexistent in the inlet region. Once phase change begins to take place, the UDF algorithm identifies cells occupied only by liquid (having zero void fraction) and loops around the identified liquid cells to calculate a volume-averaged mean liquid velocity. Using the local velocity for each vapor cell, the liquid fluctuating velocity is calculated as the absolute difference between mean liquid velocity and local vapor velocity. The agitation velocity is saved into allocated memory and recalled in the process of computing the bubble collision dispersion force, which is applied only at the interface between the liquid and vapor. To do so, the algorithm detects the liquid–vapor interface by identifying cells having a void fraction between 0 and 1. For the identified cells, agitation velocity and gradient of volume fraction of vapor, $\nabla\alpha$, are used to calculate the force, according to Eq. (22), which is incorporated as a source term in the momentum conservation equation.

3.6. Computational domain and grid independence test

Fig. 4 shows schematics of the computational domain employed in this study. The domain simulates actual test section geometry of the experiment described in Section 2. The domain is a two-dimensional axisymmetric center cut surface of a cylindrical tube having inner radius of 4.25 mm, heated length of 680 mm, and additional adiabatic length of 250 mm, the latter, which is not shown in Fig. 4, is intended to prevent unwanted exit effects. Note that using an axisymmetric domain can significantly reduce the computational cost of the simulations while accurately representing the cylindrical tube geometry of the experimental test section. The computational domain includes a solid zone of 0.5-mm thick stainless steel, mimicking the tube wall thickness from the actual test section geometry of the experiment, which allows capture of conjugate heat transfer from solid to fluid. A quadrilateral mesh is applied to the entire computational domain using ANSYS ICEM. Non-uniform mesh sizes are utilized with refinement near the wall not only to accurately capture fluid-thermal interactions in the viscous sublayer but also the micro-nucleation happening from vapor embryos in the wall region.

Grid sensitivity is tested to ensure grid independency of the model. Four different grids are constructed with four different cell sizes near the wall as shown in Table 4. For the grid independence test, intermediate operating conditions having mass velocity of 804 kg/m^{2}s, inlet subcooling of 3.32 K, and heat flux of 30.49 kW/m^2, were selected to represent overall test conditions. For each grid size, the area averaged heated wall temperature following quasi-steady convergence is compared to experimental data. Fig. 5(a) shows asymptotic convergence of average wall temperature is achieved for near wall cell size below 6 μm. In this study, 100 μm is used for the bulk region decreasing to 4 μm near the wall.

When using a turbulence model, it is crucial to adopt an acceptably low value for non-dimensional distance from the wall, which is defined as

$$y^+ = \frac{yu^\tau}{\upsilon_f} \tag{25}$$

where y, u_τ, ν_f are distance from the wall, friction velocity, and liquid kinematic viscosity, respectively. Low-Re turbulent models such as k-ω SST, which is adopted in the present simulations, aim to resolve the viscous sublayer, and therefore require that y^+ be smaller than thickness of the laminar sublayer of $y^+ = 5$. This is also important when simulating flow boiling situations like the present, where capturing heat transfer interactions in the viscous sublayer is vital to accurate prediction of bubble initiation and growth. As shown in Fig. 5(b), with the selected

Table 4
Summary of grid independence test.

	Case a	Case b	Case c	Case d
Grid size	4 μm	6 μm	10 μm	20 μm
Cell number in mesh	914,616	832,814	720,314	607,814
Converged average T_w	98.78	98.79	98.97	99.88

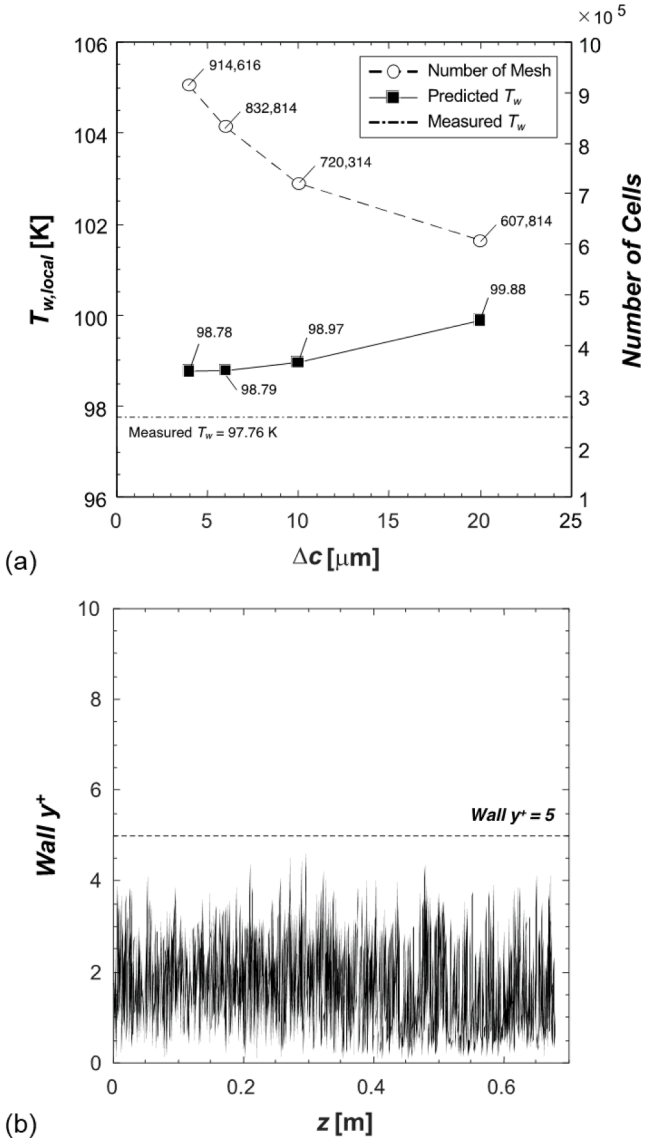

Fig. 5. (a) Effects of near-wall grid size on predicted average wall temperature and number of cells. (b) Variation of non-dimensional distance from the wall along heated length for selected grid size.

grid, wall y^+ values are below 5 along the entire heated length, satisfying the highlighted requirement.

3.7. Initial and boundary conditions

In this study, six different LN_2 flow boiling cases are simulated as indicated in Table 5, mimicking actual test conditions. According to the measurement uncertainties specified in Table 3, the variations in input parameters due to these uncertainties are extremely small when compared to the wide range of input parameters presented in Table 5. Therefore, the impact of input parameter uncertainty on the final CFD predictions is negligible. Also note that pre-calculated fully developed velocity profiles corresponding to each mass velocity (G=526, 804 kg/m^{2}s) and accompanying turbulent properties are applied at the fluid domain's inlet as boundary conditions. A no-slip condition is applied to all wall boundaries. In CLSVOF, wall adhesion angle, which influences surface normal and curvature in cells near the wall, is specified via the surface tension model used. In this study, the wall adhesion angle between vapor–solid interface and vapor–liquid interface is specified at 172.5° for LN_2 [55]. Interfaces between solid and fluid domains are applied with a coupled heat flux condition to capture conjugate heat transfer. Inlet velocity and outlet pressure are adopted, respectively, as inlet and outlet boundary conditions. Table 6 provides LN_2 property values used in the simulations, which are saturation values based on measured pressure. For all six test cases, liquid initially fully occupies the entire domain with fully developed velocity corresponding to each mass velocity case. Numerical stability is maintained by employing a global Courant number of 0.7 and using adaptive time-step scheme with the minimum and maximum time step setting of 10^{-5} and 10^{-9} s, respectively. Table 7 provides details of the numerical scheme adopted in the computations.

4. Results and discussion

4.1. Validation of computed results

To validate the accuracy of the current CFD model, predicted wall temperatures from the simulations are compared to measured wall temperatures acquired from the experimental study conducted by the present authors [43]. Fig. 6 displays both measured and predicted wall temperature profiles along the heated test section for six distinct cases. Fig. 6(a) presents comparison results for three different heat flux conditions of 13% CHF, 37% CHF, and 70% CHF under low mass velocity condition of G = 526 kg/m^{2}s. Fig. 6(b) shows comparison results for three different heat flux conditions of 11% CHF, 30% CHF, and 65% CHF under high mass velocity conditions of G = 804 kg/m^{2}s. Each sub-plot includes three predicted wall temperature profiles, depicted by distinct colored solid lines, alongside experimentally measured wall temperature data points represented by three different shape symbols. Note that predicted wall temperature results are time averaged for 1 s after achieving steady state convergence. Also, notice the error bars presented for the measured wall temperature datapoints, indicating an uncertainty range of ± 0.5°C, which confirms the accuracy of the model validation.

Table 5
Operating conditions of present simulations.

	Fluid	Mass velocity [kg/m^{2}s]	Inlet Pressure [MPa]	Wall heat flux [W/m^2]	Inlet subcooling [K]
Case 1	LN_2	526	0.41	12.56	3.46
Case 2	LN_2	526	0.41	35.64	3.46
Case 3	LN_2	526	0.41	66.35	3.46
Case 4	LN_2	804	0.55	11.03	3.32
Case 5	LN_2	804	0.55	30.49	3.32
Case 6	LN_2	804	0.55	66.32	3.32

In the case of low mass velocity, depicted in Fig. 6(a) for 13% and 37% CHF cases, both the measured and predicted wall temperature profiles indicate nearly constant wall temperatures, highlighting the dominance of the nucleate boiling heat transfer mechanism in cryogenic flow boiling physics. Concurrently, the predicted wall temperature results demonstrate exceptional performance, with average deviations of 1.7 and 1.3 K, and maximum deviations of 2.8 and 2.4 K, for 13% and 37% CHF, respectively. However, under the highest heat flux condition of 70% CHF, the predicted wall temperature profile shows slightly higher levels compared to the measured values, particularly in the downstream region, resulting in an average deviation of 1.7 K but a larger maximum deviation of 3.3 K. For high mass velocity cases, as shown in Fig. 6(b), similar trends in predictions are observed, resulting in average deviations of 1.0, 0.7, and 1.7 K, and maximum deviations of 1.5, 1.7, and 4.6 K, for 11%, 30%, and 65% CHF, respectively. It is evident that more accurate predictions are acquired for cases with higher mass velocity. Nevertheless, the overall accuracy of the current CFD model is outstanding.

The larger deviations observed for the highest heat flux can be attributed to several factors. First, despite the inclusion of additional momentum sources to address under-represented phase interactions during flow boiling, single-equation models like VOF or CLSVOF encounter challenges at high heat flux conditions, where the accumulation of vapor effectively insulates the heated wall, artificially raising the wall temperature [48]. Second, the current values of r_i may not universally cover the range of operating conditions for heat flux. Molecular dynamics simulation results reported by Liang et al. [56] indicate that the mass accommodation factor in Schrage model [57] or Tanasawa model [58] should decrease with increasing temperature. Considering that the Lee model is a derivative of the Schrage model [57], it is evident that the $r_{i,evap}$ value should also decrease with rising temperature. Nevertheless, in the present CFD model, the same $r_{i,evap}$ value is applied to all the cases, covering a wide range of heat flux conditions, in pursuit of computational simplicity and numerical stability. However, in future studies, the consideration of variable $r_{i,evap}$ values will be explored to further enhance the prediction accuracy of the CFD model. Despite the observed deviations, Fig. 6 demonstrates the excellent accuracy of the current CFD model, affirming its reliability and usefulness for simulating cryogenic flow boiling. Note that $r_{i,cond}$ is relatively less sensitive for near-saturated flow boiling cases since inlet liquid state is almost at near-saturated conditions with small inlet subcooling, which ensures minimal potential for vapor recondensation.

4.2. Predicted flow contours and void fraction

In cryogenic experiments, visualizing the two-phase flow structure along the heated test section poses significant challenges. The difficulty arises from the use of heaters that cover the entire tube for uniform heating and the implementation of a vacuum chamber designed to minimize heat gain from the ambient environment. The limitations in visualizing flow regime development in experimental studies often impedes researchers' capability to analyze the heat transfer characteristics of cryogens in conjunction with two-phase flow regimes or structures [43]. It is important to note that the mechanisms of two-phase heat transfer are intricately conjugated with two-phase flow structures and interfacial behaviors. Thus, in the pursuit of comprehensive understanding of cryogenic two-phase flow and heat transfer physics, CFD simulations emerge as invaluable prediction/design tools. This section presents and analyzes simulated results for cryogenic two-phase flow contours, as well as axial and radial void fraction profiles, considering six different operating conditions.

4.2.1. Two-phase flow contours

In Fig. 7, the predicted flow contours of LN_2 flow boiling simulations are presented for two distinct mass velocities, each associated with three

Table 6
Thermophysical properties used in the simulations.

Fluid	P	T_{sat}	h_{fg}	ρ_f	$c_{p,f}$	k_f	μ_f	ρ_g	$c_{p,g}$	k_g	μ_g	σ
	[MPa]	[K]	[J/kmol]	[kg/m^3]	[J/kg.K]	[W/m.K]	[kg/m.s]	[kg/m^3]	[J/kgK]	[W/mK]	[kg/m.s]	[N/m]
LN_2	0.41	91.6	4.97x10^6	736.5	2161.5	0.1166	9.76x10^{-5}	17.2	1293.8	0.0091	6.62x10^{-6}	0.0058
LN_2	0.55	95.3	4.79x10^6	716.8	2217.2	0.1094	8.73x10^{-5}	22.7	1369.0	0.0098	6.96x10^{-6}	0.0050

Table 7
Discretization method used in the simulations.

Variable	Discretization method
Pressure-velocity coupling	Pressure-implicit with splitting of operators (PISO)
Gradient	Least square cell based
Pressure	Body force weighted
Momentum	Second order upwind
Volume fraction	Geo-reconstruct
Turbulent kinetic energy	First order upwind
Specific dissipation rate	First order upwind
Energy	Second order upwind
Level-set function	First order upwind
Transient formulation	First order upwind

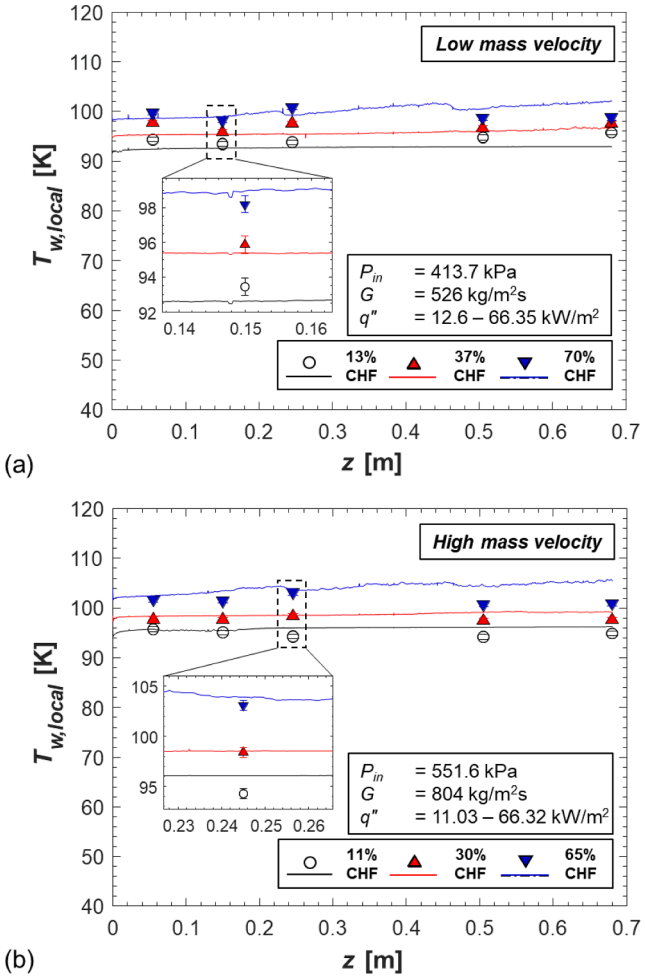

Fig. 6. Comparison of measured axial variation of wall temperature with predictions from present CFD simulations for (a) low mass velocity (G=526 kg/m^{2}s) and (b) high mass velocity (G=804 kg/m^{2}s) each with three different wall heat fluxes.

different CHF percentages. Note that CHF percentages are calculated using Eq. (26).

$$\%CHF = \frac{q''_{meas}}{q''_{CHF}} \times 100[\%] \tag{26}$$

Additionally, the simulation results presented in Fig. 7 are obtained after reaching steady state.

In Fig. 7(a), predicted flow contours for the upstream region (z = 0 – 0.1 m) are presented. For the lowest heat flux (13% CHF) and low mass velocity (G = 526 kg/m^{2}s), the onset of nucleate boiling (ONB) occurs between z = 0.03 and 0.04 m, as indicated with the red arrow. Notice that ONB under the lowest heat flux condition takes place at a relatively delayed axial location compared to those under higher heat flux conditions. Reflecting this trend, ONB occurs at much earlier axial locations near the inlet for 37% and 70 % CHF. Moreover, owing to the low wall superheat at 13% CHF, the predicted bubble growth rate is relatively slow compared to higher heat flux conditions. Accordingly, the predicted flow regime is discrete bubbly, wherein the generated tiny bubbles are confined primarily to the near-wall region. As heat flux increases from 13% to 37% CHF, the elevated wall superheat leads to more aggressive production of vapor along the tube, accompanied by a faster bubble growth rate. By further increasing heat flux to 70% CHF, larger bubbles are produced, and they coalesce with neighboring bubbles on the wall, resulting in even larger vapor structures. Notice that under the low mass velocity condition (G = 526 kg/m^{2}s), irrespective of the heat flux conditions, a significant portion of the produced bubbles is confined to the near-wall region. This phenomenon is a result of the combined effect of condensation from the colder bulk fluid and weaker shear lift force, as well as weaker bubble collision dispersion force resulting from weak flow inertia. In contrast, under the high mass velocity condition (G = 804 kg/m^{2}s), it is evident that nucleated bubbles are more easily detached from the heated wall due to the stronger shear lift force and bubble collision force resulting from stronger flow inertia. Some bubbles even travel across the tube towards the center core, as depicted for the case of 65% CHF. Furthermore, due to the enhanced single-phase liquid convection under high mass velocity, a longer heated length is required to achieve ONB. This explains the absence of bubble nucleation within the flow contour at 11% CHF under high mass velocity.

In Fig. 7(b), the predicted flow contours for the middle region (z = 0.2 – 0.3 m) reveal a substantial increase in both vapor size and population within the tube compared to those in Fig. 7(a). This signifies the development or transition of the flow regime along the axial direction. At the lowest heat flux (13% CHF) and low mass velocity (G = 526 kg/m^{2}s), the flow regime transitions from discrete bubbly to bubbly. Here, medium-sized bubbles at the core coexist with newly produced tiny bubbles in the near-wall region. At the intermediate heat flux (37% CHF) and low mass velocity (G =526 kg/m^{2}s), the predicted flow contour illustrates a flow regime transition from bubbly to slug. This is characterized by the active detachment and migration of large bubbles from the heated wall towards the central core, where they accumulate and merge to form larger oblong vapor structures. At the highest heat flux (70% CHF) and low mass velocity (G = 526 kg/m^{2}s), slug flow is dominant, characterized by the presence of large oblong vapor bubbles resulting from active bubble coalescence. In comparison to the low mass velocity cases, high mass velocity (G = 804 kg/m^{2}s) cases generally exhibit a lesser amount of vapor and smaller-sized vapor structures. This can be attributed to faster bubble detachment assisted by stronger shear

Upstream Region				
	G [kg/m²s]	P_{in} [kPa]	ΔT_{sc} [K]	q''_{CHF} [kW/m²]
Low G	526	482.6	3.5	94.95
High G	804	551.6	3.3	102.77

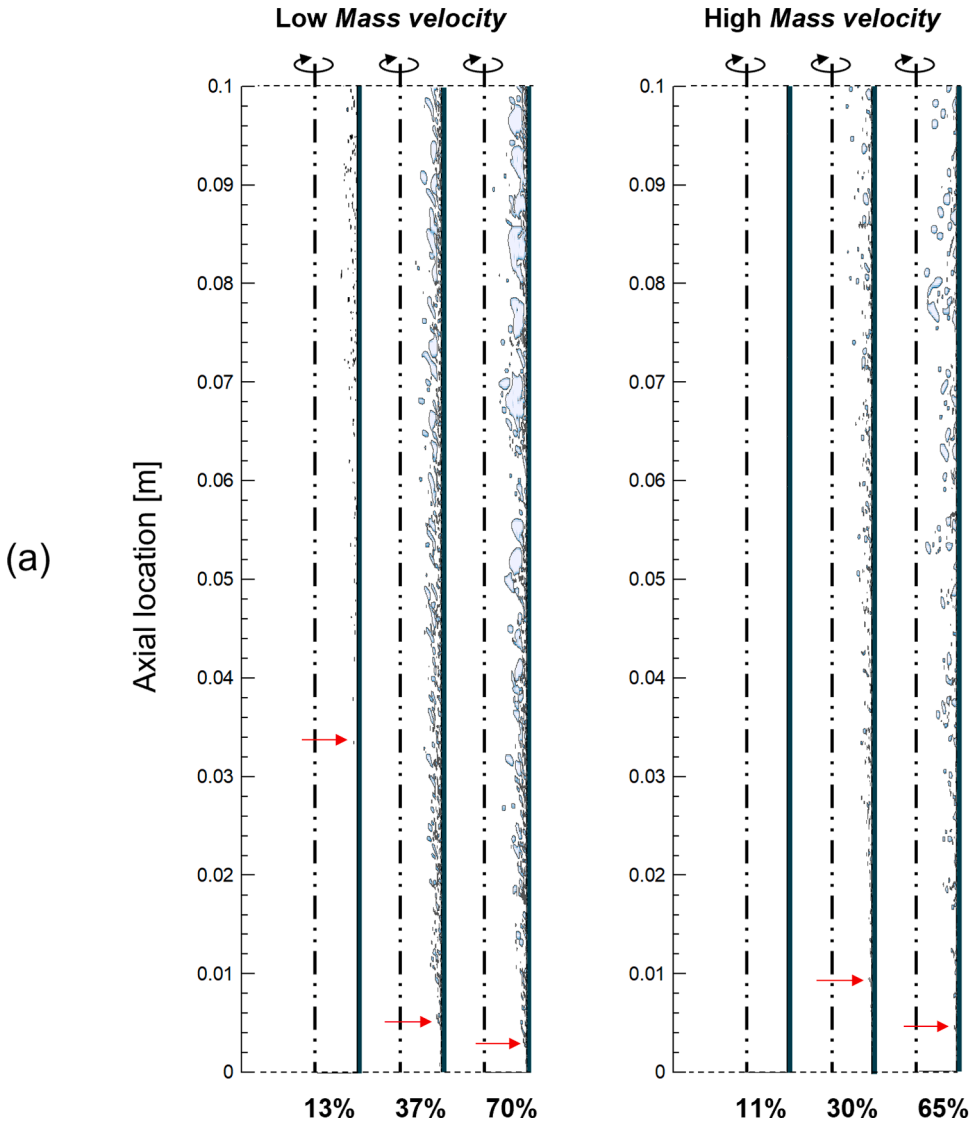

Fig. 7. Computationally predicted flow visualization images of entire heated channel for different heat fluxes at (b) middle region.

lift force resulting from the higher flow inertia, which inhibits bubbles from growing by shortening the time duration for bubbles to expand through phase change while attached to the heated wall. It is worth pointing out the ONB captured at 11% CHF and high mass velocity occurs far downstream in comparison to the ONB at 13% CHF and low mass velocity, as indicated with the red arrows.

In Fig. 7(c), predicted flow contours for the downstream region (z = 0.5 – 0.6 m) are presented, elucidating the continued evolution of flow regime. At the lowest heat flux (13% CHF) and low mass velocity (G = 526 kg/m^{2}s), a discernible flow regime transition from slug to annular is apparent. This transition is characterized by the presence of an elongated thick vapor core and an annular liquid film. Within the same flow contour, notable characteristics of cryogenic flow boiling are simulated, specifically the active generation of vapor bubbles within the liquid annular film, as indicated in the red box. As documented in previous cryogenic experimental studies [41–43], the persistent bubble nucleation within the annular liquid film stands out as a distinctive feature of cryogens. This phenomenon can be attributed to the low surface tension and low latent heat of vaporization of cryogens, requiring only a modest superheat to initiate bubble nucleation. This inherent attribute renders cryogens resilient to the suppression of nucleate boiling, even within the annular flow regime. At higher heat

Middle Region				
	G [kg/m²s]	P_{in} [kPa]	ΔT_{sc} [K]	q''_{CHF} [kW/m²]
Low G	526	482.6	3.5	94.95
High G	804	551.6	3.3	102.77

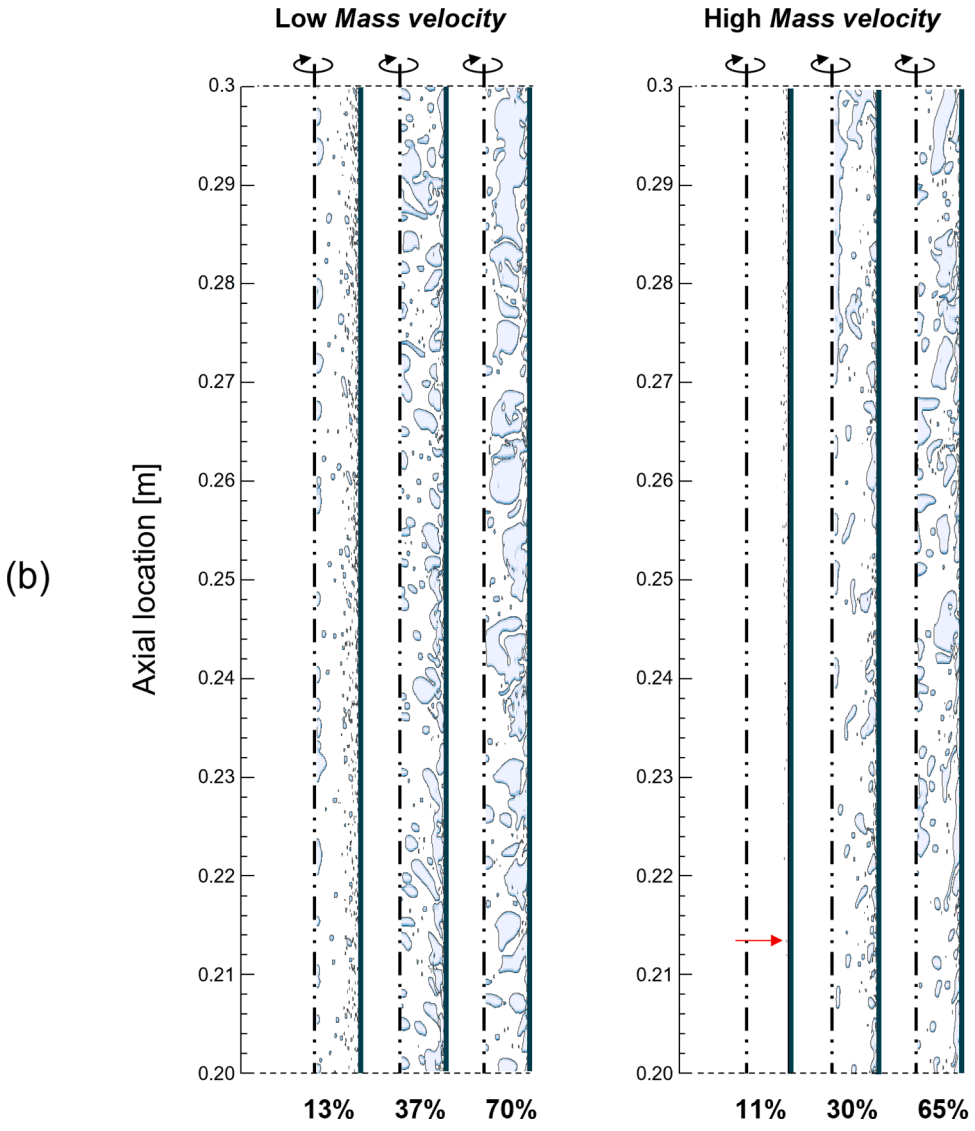

Fig. 7. (*continued*).

flux conditions of 37% and 70% CHF and low mass velocity ($G = 526$ kg/m^{2}s), more chaotic flow structures can be observed, characterized by a larger amount of vapor generation producing thicker and longer vapor chucks that travel along the tube. The significant influence of mass velocity becomes evident when comparing cases with the two different mass velocities at the lowest heat flux. Despite the similar CHF percentages, the flow regime remains in discrete bubbly flow under high mass velocity. The increased flow inertia intensifies the effect of shear lift force, leading to more frequent detachment of smaller-sized bubbles. As the thermal boundary layer expands along the tube, small bubbles migrate toward the core, but their penetration beyond the thermal boundary layer is impeded by lingering condensation effects from the colder bulk fluid. At the elevated heat flux percentages of 30% and 65% CHF and high mass velocity ($G = 804$ kg/m^{2}s), the predicted flow structures exhibit similarities to those observed under low mass velocity ($G = 526$ kg/m^{2}s), with the following distinctions: (a) vapor structures are smaller and thinner, attributed to the intensified shear lift force effect, (b) a broader surface area of liquid contacts the heated wall, indicating enhanced liquid replenishment under high mass velocity, and (c) a less wavy liquid–vapor interface. Note that less wavy interface at high mass velocity was also experimentally captured and reported in previous cryogenic flow boiling studies [43].

Downstream Region				
	G [kg/m²s]	P_{in} [kPa]	ΔT_{sc} [K]	q''_{CHF} [kW/m²]
Low G	526	482.6	3.5	94.95
High G	804	551.6	3.3	102.77

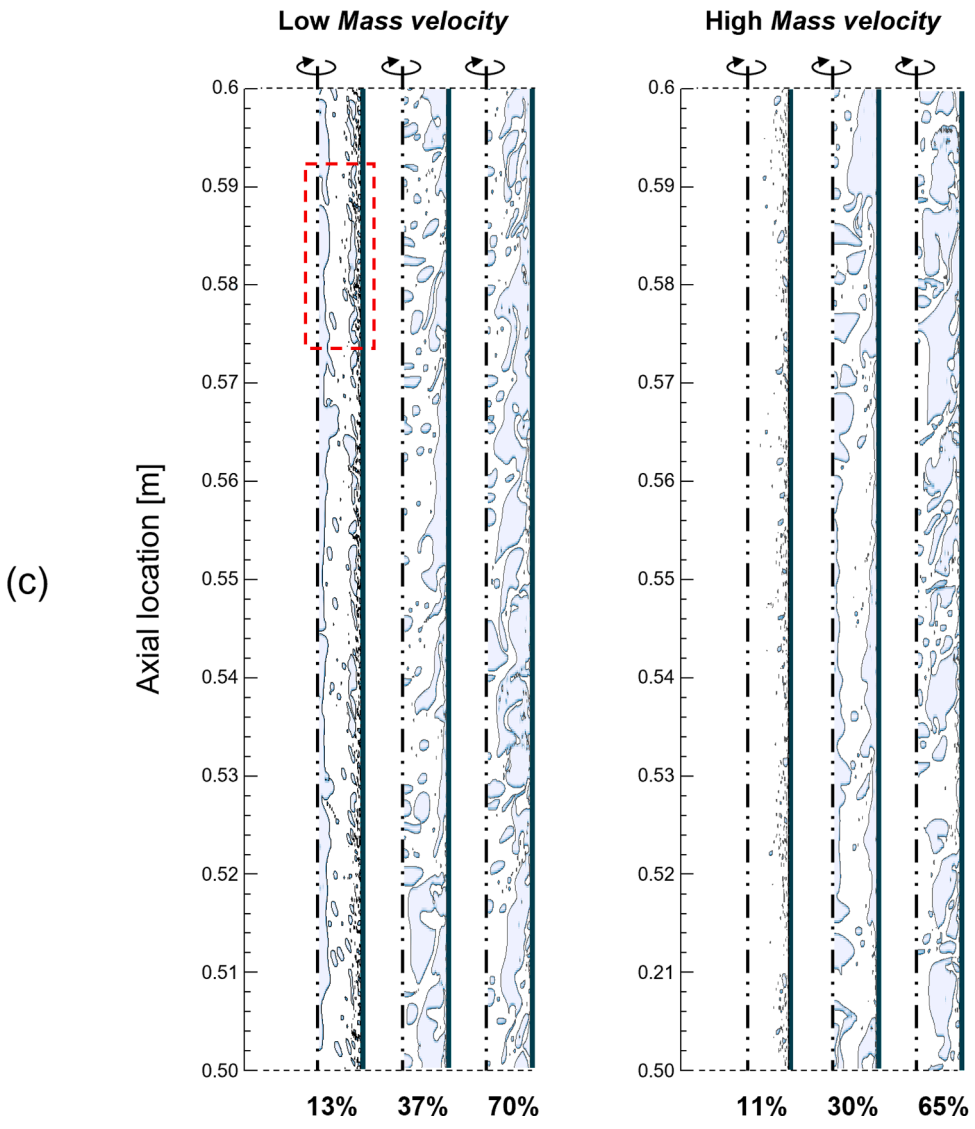

Fig. 7. (*continued*).

4.2.2. Axial void fraction profiles

Fig. 8 presents a comparative analysis of void fraction predictions obtained through two distinct methods: Fig. 8(a) and 8(b) depict results acquired from the CFD simulations, while Fig. 8(c) and 8(d) illustrate calculations from empirical correlations utilizing Levy's correlation [59], and Zivi [60]'s correlations. In the present study, x is calculated from x_e using the following expression by Levy [59], Note that experimentally acquired equilibrium quality, using Eq. (3), and thermal properties acquired based on experimentally acquired local pressure, were utilized as input parameters for correlation predictions.

$$x(z) = x_e(z) - x_d(z) exp\left\{\frac{x_e(z)}{x_d(z)} - 1\right\} \tag{27}$$

where $x_d(z)$ is the value of x_e at the point of bubble detachment, which is negative and given by

$$x_d(z) = -\left[\frac{c_{p,f}\Delta T_d(z)}{h_{fg}}\right] \tag{28}$$

$$\text{where } T_d(z) = q''(z)\left[\frac{1}{h_{fo}} - \frac{T_B^+}{\rho_f c_{p,f} u^*}\right] \tag{29}$$

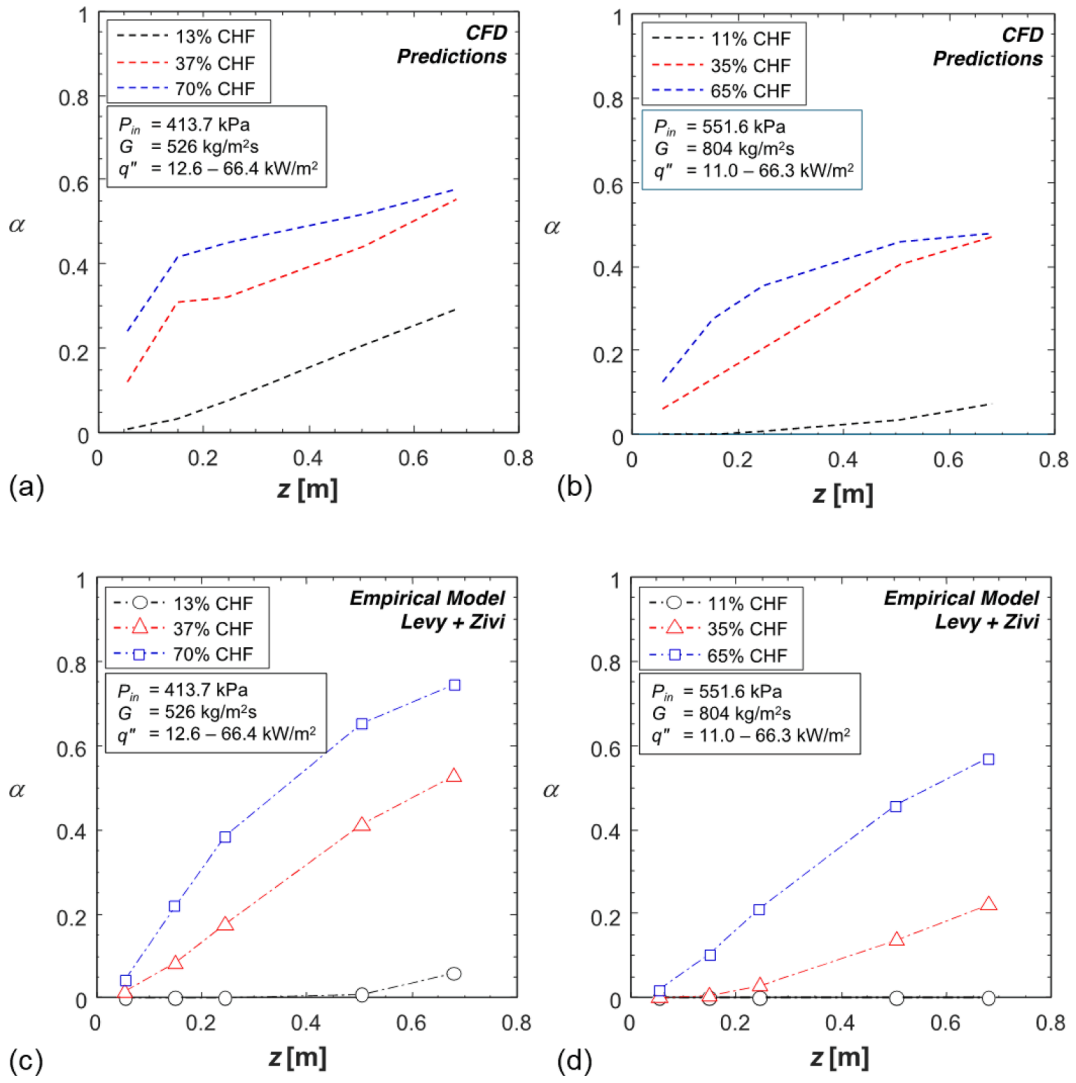

Fig. 8. Area-averaged axial void fraction profiles from CFD predictions under (a) low mass velocity condition and (b) high mass velocity condition, and area-averaged void fraction predictions from empirical correlations under (c) low mass velocity condition and (d) high mass velocity condition, each with three different wall heat fluxes.

$$T_B^+ = Pr_f Y_B^+ \quad \text{for} \quad 0 \le Y_B^+ \le 5 \tag{30a}$$

$$T_B^+ = 5\left[Pr_f + ln\left\{1 + Pr_f\left(\frac{Y_B^+}{5} - 1\right)\right\}\right] \text{for} \, 5 \le Y_B^+ \le 30 \tag{30b}$$

$$T_B^+ = 5\left[Pr_f + ln(1 + 5Pr_f) + 0.5ln\left(\frac{Y_B^+}{5}\right)\right] \text{for} \, 30 \le Y_B^+ \tag{30c}$$

$q^{''}$, Y_B^+ and u^* in the above relations are the heat flux based on heated perimeter of the channel, nondimensional distance to the tip of the vapor bubble, and friction velocity; the latter two are given, respectively, by

$$Y_B^+ = Y_B\sqrt{\frac{\tau_w}{\rho_f}}\frac{\rho_f}{\mu_f} = 0.015\left(\frac{\sigma D}{\tau_w}\right)^{0.5}\sqrt{\frac{\tau_w}{\rho_f}}\frac{\rho_f}{\mu_f} = 0.015\frac{(\rho_f \sigma D)^{0.5}}{\mu_f} \tag{31}$$

$$u^* = \sqrt{\frac{\tau_w}{\rho_f}} = \sqrt{\frac{f_o}{2}}\frac{G}{\rho_f} \tag{32}$$

Then, based on the acquired x, void fraction is calculated using the following expression by Zivi [60],

$$\alpha = \left[1 + \left(\frac{1 - x_e}{x_e}\right)\left(\frac{\rho_g}{\rho_f}\right)^{2/3}\right]^{-1} \tag{33}$$

Given that these empirical correlations originate from conventional fluid systems, particularly water, it is essential to note the uncertainty surrounding their applicability in the context of cryogenic flow boiling. Nevertheless, the combination of Levy and Zivi correlations was utilized, and corresponding results were compared with the predictions obtained from CFD simulations.

As witnessed from the predicted flow contours in Fig. 7(a)–(c), the predicted void fraction profiles in Fig. 8(a) and 8(b) demonstrate monotonically increasing trends along the axial direction, progressing from upstream to downstream of the heated tube. Furthermore, the predicted void fraction profiles manifest an upward shift with increasing heat flux, suggesting a greater amount of vapor generation, accelerated bubble growth, and active bubble coalescence under elevated heat flux conditions along the tube. Mirroring the observed mass velocity effect discussed in Fig. 7, the void fraction profiles under high mass velocity, Fig. 8(b), generally exhibit lower magnitudes of void fraction compared to those under low mass velocity, Fig. 8(a). Analogous trends are projected by the empirical correlations, albeit with a notable distinction. The empirical correlations forecast a significantly lower void fraction in

comparison to CFD under low heat flux conditions, as illustrated for 13% CHF in Fig. 8(c) and 11% CHF in Fig. 8(d). This deviation arises from the empirical correlations' incapacity to discern non-equilibrium effects within the subcooled flow boiling region. Even under near-saturated inlet conditions of the current cases, the existence of a radial temperature gradient across the cross-section of the tube can lead to bubble nucleation in the near-wall region, especially in the upstream region where bulk fluid temperature is still below saturation temperature. However, the empirical correlations, which predominantly rely on 1-D energy balance, are unable to differentiate the presence of bubbles in multi-dimensional surface or volume. Consequently, such disparities between predictive methods may occur. Nevertheless, the two prediction methods provide fair agreement both quantitatively and qualitatively. A summary of quantitative comparison results are provided in Table 8. The influence on the quantified difference exerted by experimental uncertainties are also provided in Table 8. Difference A represents the standard difference between the correlation predicted void fraction and the CFD predicted void fraction, $\alpha_{corr} - \alpha_{CFD}$. Meanwhile, Difference B, $\alpha_{corr,min} - \alpha_{pred}$, and Difference C, $\alpha_{corr,max} - \alpha_{pred}$, indicate the deviations from the predicted void fraction to the minimum and maximum correlation predicted void fractions, respectively, accounting for propagated experimental uncertainty.

Table 8
Summary of comparison between predicted and measured void fraction.

Z [m]	α_{exp}	α_{pred}	Difference ($\alpha_{corr} - \alpha_{pred}$)	Difference ($\alpha_{corr,min} - \alpha_{pred}$)	Difference ($\alpha_{corr,max} - \alpha_{pred}$)
CASE 1					
0.055	0	0.007	−0.007	−0.007	−0.007
0.150	0	0.032	−0.032	−0.032	−0.032
0.245	0	0.075	−0.075	−0.075	−0.075
0.505	0.008	0.207	−0.199	−0.200	−0.199
0.680	0.058	0.293	−0.235	−0.237	−0.232
CASE 2					
0.055	0.013	0.120	−0.107	−0.108	−0.107
0.150	0.080	0.309	−0.229	−0.233	−0.225
0.245	0.172	0.321	−0.149	−0.157	−0.142
0.505	0.409	0.442	−0.033	−0.052	−0.015
0.680	0.524	0.553	−0.029	−0.053	−0.006
CASE 3					
0.055	0.044	0.240	−0.196	−0.198	−0.194
0.150	0.217	0.415	−0.198	−0.208	−0.188
0.245	0.384	0.450	−0.066	−0.083	−0.049
0.505	0.651	0.517	0.134	0.104	0.163
0.680	0.743	0.577	0.166	0.133	0.200
CASE 4					
0.055	0	0	0	0.000	0.000
0.150	0	0	0	0.000	0.000
0.245	0	0.007	−0.007	−0.007	−0.007
0.505	0	0.034	−0.034	−0.034	−0.034
0.680	0	0.072	−0.072	−0.072	−0.072
CASE 5					
0.055	0	0.060	−0.060	−0.060	−0.060
0.150	0.005	0.132	−0.127	−0.127	−0.126
0.245	0.028	0.204	−0.176	−0.177	−0.175
0.505	0.136	0.405	−0.269	−0.275	−0.262
0.680	0.220	0.471	−0.251	−0.261	−0.241
CASE 6					
0.055	0.018	0.126	−0.108	−0.109	−0.107
0.150	0.101	0.275	−0.174	−0.178	−0.169
0.245	0.208	0.354	−0.146	−0.155	−0.136
0.505	0.454	0.458	−0.004	−0.025	0.016
0.680	0.565	0.479	0.087	0.061	0.112

4.2.3. Radial void fraction profiles

Fig. 9 presents CFD predicted radial void fraction profiles at five axial locations along the heated tube. These profiles are derived for the two mass velocities and three heat flux conditions, the latter corresponding to approximately 10%, 30%, and 70% CHF. Time averages for the void fraction are obtained over a period of 1 s. Within each sub-figure, the radial area occupied by the heated wall region is indicated as red-colored band.

In Fig. 9(a), radial void fraction profiles are presented for the case with a mass velocity of $G = 526$ kg/m^{2}s and 13% CHF. At axial locations near the inlet, $z = 55$ and 150 mm, the void fraction profiles exhibit nearly zero values across the heated tube. There is a slight increase at the heated wall, attributed to newly produced tiny bubbles that are attached to, but have not yet departed from, the heated wall. At $z = 245$ mm, multiple peaks begin to appear within the radial void fraction profile, indicating the departure and migration of vapor bubbles away from the heated wall. At a downstream location of $z = 505$ mm, two prominent peaks characterized by elevated void fraction magnitudes are discernible: one in close proximity to the heated wall and another positioned at the center core. The peak located at the center core is indicative of the accumulation and coalescence of vapor bubbles towards the central axis. Notice the gradual decrease of void fraction within the radial range of $r = 0$ to 2 mm, marking the span of the center vapor core. Near to the heated wall, an additional void fraction peak is evident, signifying the ongoing process of active bubble nucleation within the surrounding liquid film. As elucidated in Fig. 7(c) and emphasized in experimental studies of cryogenic flow boiling [41–43], the low surface tension and low latent heat of vaporization of cryogens contribute to the bubble nucleation persisting even within the annular film. Apparently, it is assuring that the current CFD model is proficient in accurately capturing this cryogenic phenomenon. Under the operating condition of higher mass velocity of $G = 804$ kg/m^{2}s and 11% CHF, Fig. 9(b), radial void fraction profiles exhibit a nearly flat trend near $\alpha = 0$ for all axial locations. This observation corroborates the impact of increased flow inertia effectively suppressing bubble nucleation. Observing the marginal rise in void fraction within the profiles at downstream locations, $z = 505$ and 680 mm, signifies the initiation of boiling. However, the subsequent processes of bubble growth, migration, and accumulation are not as pronounced as observed under the low mass velocity condition in Fig. 9(a). With an increase in heat flux percentage to 30% to 37% CHF, Fig. 9(c) and 9(d), more pronounced radial void fraction profiles become evident. In Fig. 9(c), a double-peak radial profile begins to take shape even at the most upstream location of $z = 55$ mm. Progressing downstream, starting from $z = 505$ mm, the radial profiles exhibit a relatively smoother center section with peaks toward the heated wall. The uniform section of the profile, spanning from $r = 0$ to 3 mm, signifies evenly distributed vapor structures which is a characteristic also witnessed by the flow contours in Fig. 7(c). In Fig. 9(d), under the operating condition of $G = 804$ kg/m^{2}s and 30% CHF, double-peaking radial profiles are noticeable across all axial locations. This observation signifies concurrent active vapor generation at the heated wall and active migration of bubbles toward the center, giving rise to the formation of oblong vapor structures at the core. At the highest heat flux percentages of 65% to 70% CHF, irrespective of mass velocity, a rapid escalation of void fraction is evident in both axial and radial directions, as depicted in Fig. 9(e) and 9(f). The observation of larger void fraction peaks in close proximity to the heated wall indicates the formation of a localized vapor blanket, a phenomenon anticipated to induce CHF were the heat flux is elevated further to higher values approaching 100% CHF. However, under the current heat flux conditions, as observed from the predicted flow contours in Fig. 7, there is active liquid replenishment occurring between these localized vapor pockets. This dynamic process effectively facilitates the cooling of the wall, thus preventing pre-CHF temperature excursions.

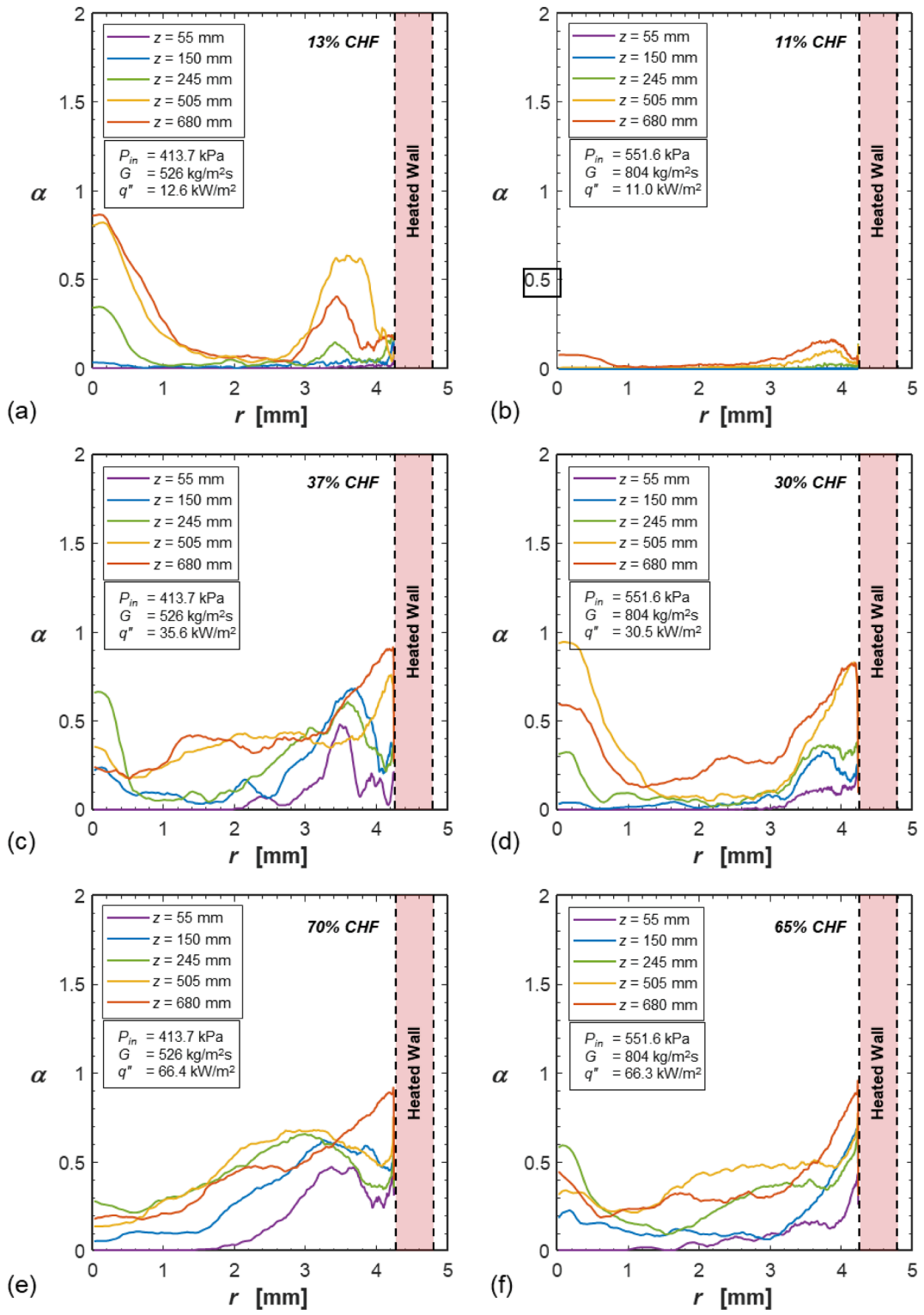

Fig. 9. Time-averaged radial void fraction profiles across the axisymmetric channel for five axial locations under different operating test conditions.

4.3. *Fluid velocity predictions*

Acceleration of fluid flow along the boiling tube is closely related to the two-phase flow structure and the evolution of void fraction. Furthermore, comprehending the two-phase flow velocity field is crucial for understanding the impact of flow inertia on two-phase heat transfer. However, experimental measurement of fluid velocity along the test section is quite challenging, particularly in the context of cryogenic flow boiling. To address this limitation, CFD simulations can assist in understanding cryogenic two-phase flow behavior by providing both axial and radial fluid velocity profiles, as demonstrated in Figs. 10 and 11. Note that the presented velocity profiles are extracted after achieving steady state and time-averaged for 1 s.

4.3.1. *Axial fluid velocity profiles*

In Fig. 10(a), axial fluid velocity profiles are provided for $G = 526$

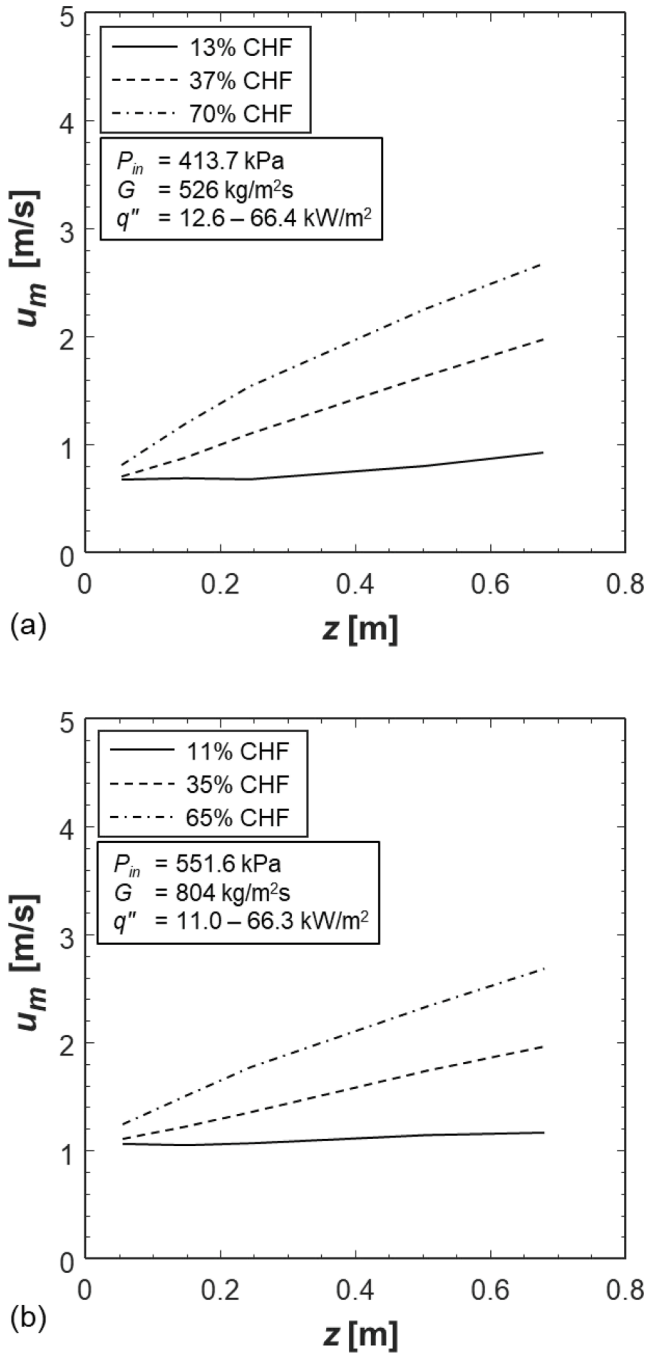

Fig. 10. Area-averaged axial fluid velocity variations along the axisymmetric tube for (a) low mass velocity (G=526 kg/m^{2}s) and (b) high mass velocity (G=804 kg/m^{2}s), each with three different wall heat fluxes.

kg/m^{2}s and three heat fluxes of 13%, 37%, and 70% CHF. Note that the axial fluid velocity profiles provided are radially averaged values for all the axial locations. Two discernible trends are evident. First, the fluid velocity exhibits an increase with axial location. Second, the slope of the axial profiles becomes more pronounced with increasing heat flux. These observed trends in velocity profiles are direct consequences of the escalating void fraction. The gradual axial augmentation of vapor void fraction under fixed heat flux, as depicted in Figs. 7 and 8, induces an axial acceleration of fluid flow to maintain the constant mass flow rate throughout the heated tube. Furthermore, the more pronounced acceleration with increasing heat flux is evidently attributed to the enhanced vapor production, accumulation, and coalescence. Fig. 10(b) shows axial fluid velocity profiles for G = 804 kg/m^{2}s and three heat fluxes of 11%, 35%, and 65% CHF. Similar axial velocity trends are observable here, despite the subdued slope of the profiles, compared to those depicted in Fig. 10(a). The diminished slope of the profiles is a direct consequence of the increased mass velocity, which effectively reduces the amount of vapor produced within the heated tube.

4.3.2. Radial fluid velocity profiles

Fig. 11 illustrates radial mixture fluid velocity profiles at five axial locations along the heated tube for the two mass velocities and three heat fluxes of approximately 10%, 30%, and 70% CHF. Here too, time averages for the mixture fluid velocity are obtained over a period of 1 s. Within each sub-figure, the radial area occupied by the heated wall region is also indicated with a red colored band.

In Fig. 11(a), predicted radial velocity profiles are provided for G = 526 kg/m^{2}s and 13% CHF. Observable are typical flow boiling velocity profiles. At upstream axial locations of z = 55 and 150 mm, minimal distortion is evident in the velocity profiles, attributed to the small size of bubbles confined to the near-wall region. However, at farther downstream locations, an increase in vapor void fraction within the tube prompts localized flow acceleration. For instance, near the outlet, specifically at z = 505 and 680 mm, flow acceleration at the center core becomes noticeable due to the development of a thick vapor core, aligning with the radial distribution of vapor structures as depicted in Fig. 9(a). In contrast to the low mass velocity profiles depicted in Fig. 11(a), the high mass velocity profiles display a considerably prolonged region of undistorted, smooth, fully developed radial velocity profiles extending to an axial location of z = 245 mm. This extension is attributed to the delayed ONB under the high mass velocity. Subsequent to the initiation of bubble nucleation at farther downstream locations, z = 505 and 680 mm, localized near-wall accelerations become evident in the velocity profiles. These localized peaks are directly correlated with the presence of vapor bubbles adjacent to the heated wall. The increased vapor production associated with the higher heat fluxes of 37% and 30% CHF leads to enhanced flow acceleration, resulting in higher velocities, as illustrated in Fig. 11(c) and 11(d), respectively. As heat flux is further increased to 70% and 65% CHF, Fig. 11(e) and 11(f), respectively, axial acceleration in the radial velocity profile becomes even more apparent. Moreover, irrespective of mass velocity, the significant vapor production, accumulation, and coalescence near the wall lead to velocity peaks in the same region.

4.4. Fluid temperature predictions

In addition to two-phase flow structures and velocity fields, another crucial thermal parameter challenging to experimentally acquire is fluid temperature. Experimental measurements typically require submerging thermocouples or RTDs within the flow. This installation can introduce significant uncertainties in cryogenic flow boiling experiments because of obstructions to the fluid flow, potential fluid leaks, and parasitic heat gain. Therefore, the installation of such instruments is commonly avoided, and instead, a theoretical energy balance method, based on inlet conditions and uniform heat flux, is employed to acquire local bulk fluid temperature information. Nonetheless, as illustrated in Fig. 8, it is evident that 1-D analytical energy balance with empirical correlations poses challenges in accurately discerning non-equilibrium effects, impairing accurate estimation of both void fraction and fluid temperature. To address these limitations and to offer physical insights into the spatial variations of fluid temperature, CFD simulations constitute a powerful alternative. In this section, the predicted axial fluid temperature profiles are compared with the measured fluid temperature profiles to assess the reliability and robustness of the current CFD model. Additionally, simulated fluid temperature field contours for each set of operating conditions are presented to understand the non-equilibrium effects based on analysis of thermal boundary layer development.

In Fig. 12, axial fluid temperature profiles are provided for G = 526

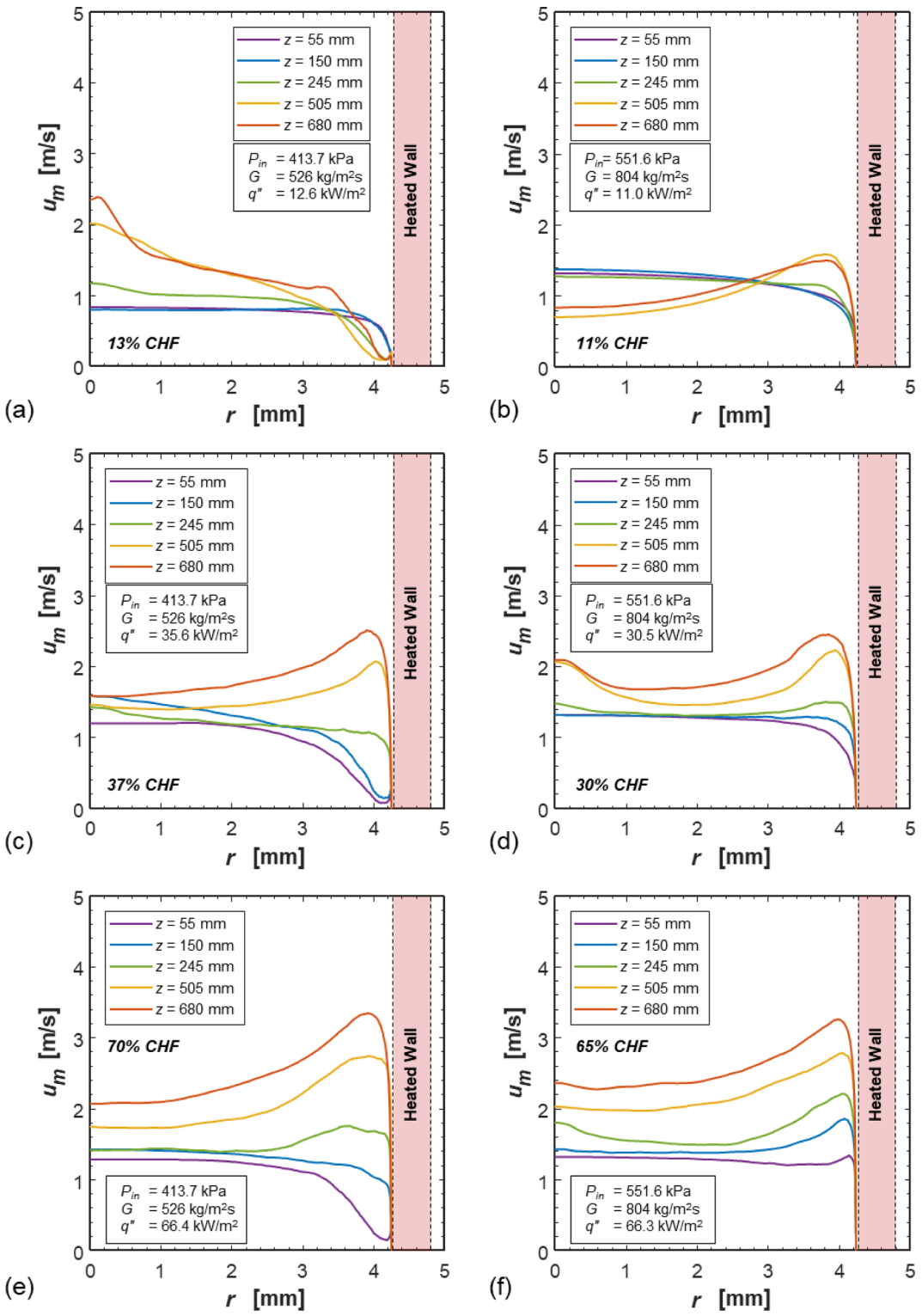

Fig. 11. Time-averaged radial mixture fluid velocity profiles across the axisymmetric channel for five axial locations under different operating test conditions.

kg/m^{2}s and three heat fluxes of 13%, 37%, and 70% CHF. Note that the axial fluid temperature profiles provided are radially averaged values for each axial location. Also provided are energy-balance-based fluid temperature profiles calculated from measured inlet temperature, mass velocity, and heat flux, using Eq. (4). From the comparison, as depicted throughout Fig. 12(a)-(c), the axial profiles using the two methods almost overlap one another for all three heat fluxes, exhibiting added validation of capability of the current CFD model in predicting the bulk fluid temperature. Also shown in Fig. 12 are CFD-predicted developing fluid temperature contours within the heated tube for the same three heat fluxes. From the contours, it is apparent that within the upstream half of the heated test section ($z = 0 – 0.3$ m), regardless of heat flux, the color maps are predominantly blue, indicating predominantly subcooled bulk fluid with emerging thermal boundary layers primarily confined to the near-wall region. As nucleated bubbles grow in size and depart from the heated wall, the heat is transported into the subcooled bulk liquid,

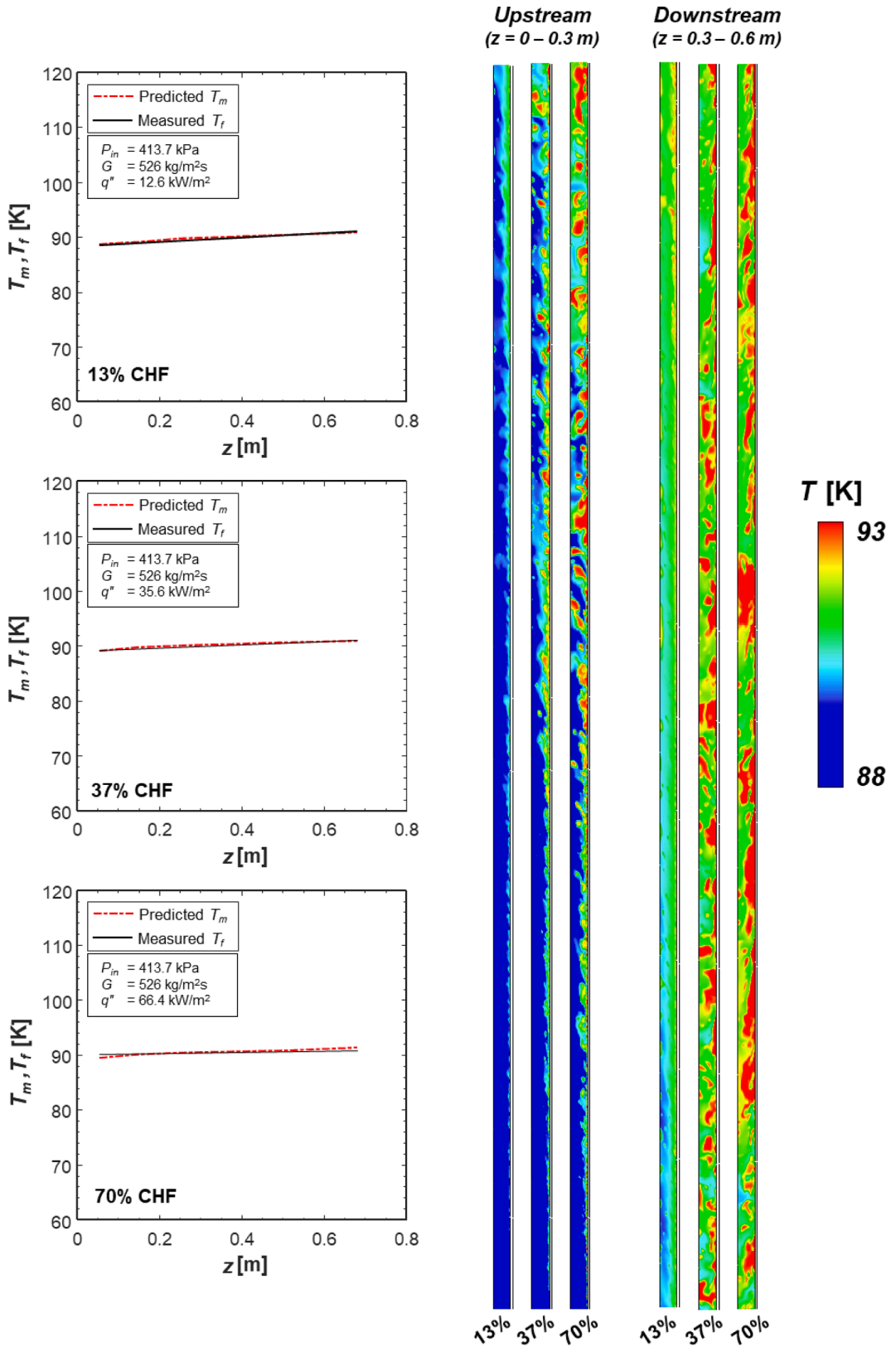

Fig. 12. Area-averaged axial fluid velocity profiles and predicted fluid temperature contours along the axisymmetric tube for low mass velocity (G=526 kg/m^{2}s) under three different heat flux conditions.

increasing the temperature of the bulk liquid. Correspondingly, the color in the temperature contours transitions into green, indicating saturated bulk liquid temperature, mainly throughout the downstream half of the heated tube ($z = 0.3 – 0.6$ m). Moreover, at 37% and 70% CHF, spurious large red patches are observable along the downstream half of the test section, indicating a development of superheated vapor chunks. Despite the presence of superheated vapor near the wall, effective liquid replenishment is still active, bringing colder liquid into contact with the heated surface. Therefore, the heated wall temperature can be adequately maintained without excursion. Based on these trends,

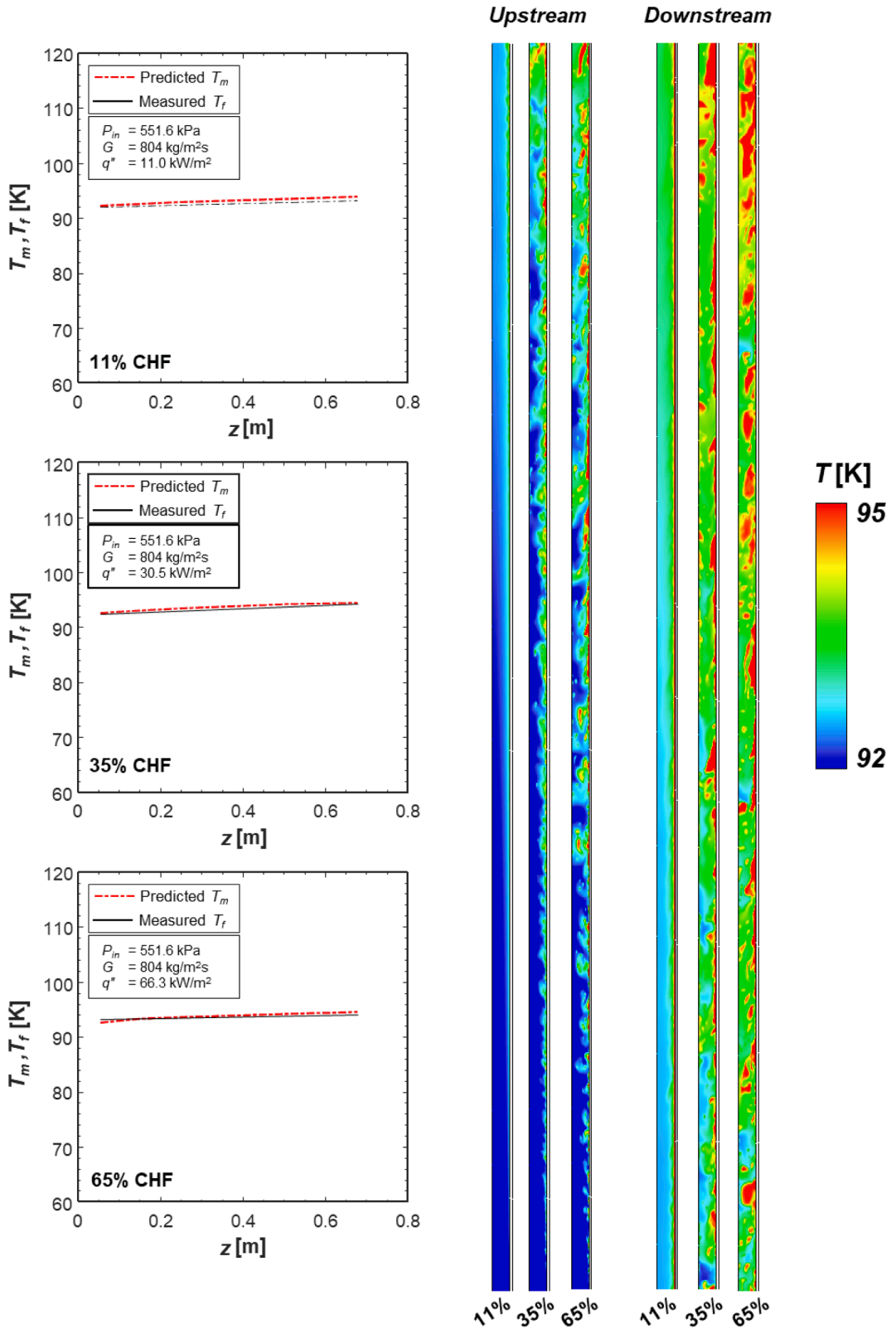

Fig. 13. Area-averaged axial fluid velocity profiles and predicted fluid temperature contours along the axisymmetric tube for high mass velocity (G=804 kg/m^{2}s) under three different heat flux conditions.

followings are the notable differences associated with increasing heat flux: (a) more chaotic expansion of thermal boundary layer, and (b) more vigorous and faster transition of colormap due to enhanced turbulent mixing and flow acceleration. In Fig. 13, axial fluid temperature profiles are provided for $G = 804$ kg/m^{2}s and three heat fluxes of 11%, 30%, and 65% CHF. Similar to Fig. 12, the CFD-predicted and energy-balance-based fluid temperature profiles in Fig. 13 show excellent agreement. Due to the enhanced flow inertia under this higher mass velocity, several notable observations are evident when compared to the low mass velocity temperature contours in Fig. 12. At 11% CHF, the lowest heat flux considered, thermal boundary layer development is extremely confined to the near wall region due to the suppressed bubble nucleation, growth, and coalescence under at the higher mass velocity, as witnessed in Fig. 7(a)-(c). Consequently, bulk fluid temperature reaches saturation temperature at extreme downstream locations of the tube, as signified by the color transition into green. Moreover, at 35% and 65% CHF, a noticeable decrease in the amount of superheated vapor structures can be observed, promoting more effective liquid contact with the heated wall. This, in turn, aids in delaying the occurrence of CHF, which is the primary reason for higher CHF under higher mass velocity.

Overall, this study clearly demonstrated outstanding capability of the current CFD model in accurate computation of (1) axial variation of wall temperature and (2) axial variation of bulk fluid temperature. Recall the fact that wall temperature, T_w, and bulk fluid temperature, T_f, are two building blocks when evaluating heat transfer coefficient for any two-phase flow boiling system. Thus, it can be concluded that the proposed CFD model has validated its ability to precisely predict cryogenic heat transfer coefficients, proving its potential to serve as a reliable alternative for designing practical two-phase cryogenic flow boiling systems in space applications.

4.5. Recommendations for future work

Despite the success of the new CFD model as a robust tool for predicting and designing cryogenic flow boiling systems, the findings from this study indicate the need for future work to further improve predictive accuracy. The followings are recommendations for future computational investigations in boiling systems:

(1) Focused study of the effects of flow orientation force on multiphase boiling simulations
(2) Focused study of the effects of reduced gravity on multiphase boiling simulations
(3) Focused study of systematic optimization process of mass intensity factor, r_i
(4) Focused study of mechanistic modeling of heterogenous bubble nucleation coupled with advanced interface tracking methods

By addressing these areas, future research can build upon the current model to achieve higher fidelity and broader applicability in predicting and designing cryogenic flow boiling systems.

5. Conclusions

The present study conducted CFD simulations of cryogenic vertical upflow boiling for two mass velocities of $G = 526$ and 804 kg/m^{2}s, each with three different heat fluxes of approximately 10%, 30%, and 70% CHF, all under Earth gravity. The CFD model employed CSLVOF interface tracking in conjunction with additional source terms of bubble collision dispersion force and shear lift force in the momentum conservation equation, with the aim of enhancing simulation accuracy. Simulated results were presented for crucial two-phase flow and thermal parameters, including the spatial variations of interfacial structure, void fraction, fluid velocity, and fluid temperature. Key takeaways from the study are as follows:

(1) Accuracy of the CFD model was assessed and validated against measured wall temperature data acquired from previous terrestrial gravity cryogenic experimental study conducted by the authors [43], showing average deviations of less than 2 K, regardless of operating conditions.
(2) From the simulated two-phase flow contours, captured flow patterns included bubbly, slug, churn, and annular
(3) By analyzing the simulated two-phase flow contours, effects of increasing heat flux include earlier instigation of ONB, pronounced bubble nucleation, faster bubble growth, aggressive bubble coalescence, and larger size of vapor structures.
(4) By analyzing the simulated two-phase flow contours, effects of increasing mass velocity include delayed instigation of ONB, suppressed bubble nucleation, faster bubble detachment, smaller bubble departure diameter, and smaller size of vapor structures.
(5) Simulated axial void fraction profiles were compared to those predicted using empirical correlations. While similar trends were realized, the CFD model showed superiority in ability to capture non-equilibrium effects in the upstream region of the heated tube.
(6) Both axial and radial variations of flow velocity were presented which reflect acceleration trends synchronized with axial and radial void fraction development, respectively.
(7) Excellent agreement was realized between CFD-predicted axial bulk fluid temperature profiles and those predicted via energy balance.
(8) Overall, the present CFD model was validated to be both highly effective and accurate in predicting two-phase transport parameters vitally important to understanding evolution of cryogenic flow boiling which are not easily accessible from experiment. This proves its potential to serve as a reliable alternative for designing practical two-phase cryogenic flow boiling systems in space applications.

Declaration of competing interest

The authors declare the following financial interests/personal relationships which may be considered as potential competing interests: [Issam Mudawar reports financial support was provided by NASA. If there are other authors, they declare that they have no known competing financial interests or personal relationships that could have appeared to influence the work reported in this paper].

Data availability

The data that has been used is confidential.

Acknowledgement

The authors are appreciative of the support of the National Aeronautics and Space Administration (NASA) under grant 80NSSC21K0500.

Appendix

A1. Heat transfer coefficient predictions

To acquire heat transfer coefficient (HTC), unlike wall temperature, it requires post-processing which inevitably induce propagation of

uncertainties. Moreover, during the calculation for heat transfer coefficient, as displayed in Eq. (6), bulk fluid temperature, T_f, information is required. Within CFD, the bulk temperature information, T_f, can be retrieved using various methods, which can significantly affect the results of error evaluation. Therefore, using wall temperature as a validation parameter is considered a more direct and precise method of model validation. In such sense, in this paper, wall temperature measurements are primarily selected for validation, and the comparison results were shown as presented in Fig. 6.

However, to present the performance of the current CFD model, here in appendices, a comparison result between measured HTC and predicted HTC is presented, as shown in Fig. A1. The comparison were conducted for case 2, in Table 5, having operating conditions of $G = 526$ kg/m^{2}s, $P_{in} = 413.7$ kPa, $\Delta T_{sub,in} = 3.46$ K, and $q" = 35.64$ kW/m^2. Note that the bulk fluid, T_f, is retrieved by area-averaging only the liquid temperature over entire fluid domain. As pointed out earlier, based on this bulk fluid calculation method, CFD prediction results for HTC can vary significantly. Nevertheless, as displayed in Fig. A1, the predicted HTC shows a good agreement with the measured HTC, further validating the validity of the current numerical model used in this study.

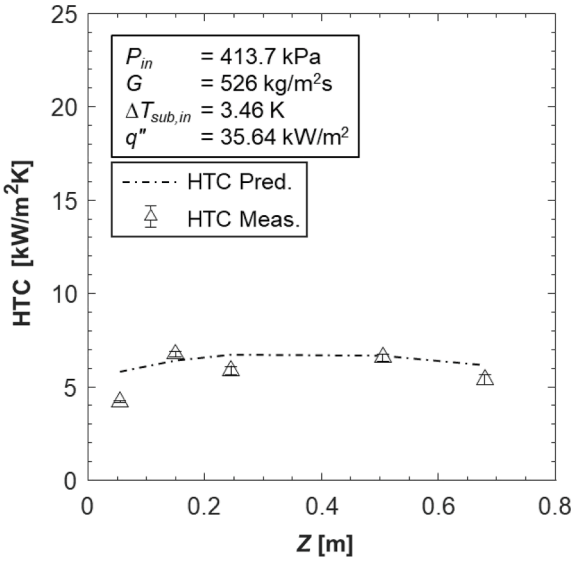

Fig. A1. Comparison between predicted and measured HTC under operating conditions of G=576 kg/m^{2}s, $P_{in} = 413.7$ kPa, $\Delta T_{sub,in} = 3.5$ K, and $q" = 35.6$ kW/m^2.

References

[1] M.K. Sung, I. Mudawar, Single-phase and two-phase heat transfer characteristics of low temperature hybrid micro-channel/micro-jet impingement cooling module, Int. J. Heat Mass Transf. 51 (2008) 3882–3895.

[2] M.K. Sung, I. Mudawar, Single-phase and two-phase hybrid cooling scheme for high-heat-flux thermal management of defense electronics, J. Electron. Packag. 131 (2009) 021013.

[3] Y. Li, H. Wu, Experiment investigation on flow boiling heat transfer in a bidirectional counter-flow microchannel heat sink, Int. J. Heat Mass Transf. 187 (2022) 122500.

[4] S. Lee, I. Mudawar, Transient characteristics of flow boiling in large micro-channel heat exchangers, Int. J. Heat Mass Transf. 103 (2016) 186–202.

[5] S. Lee, V.S. Devahdhanush, I. Mudawar, Frequency analysis of pressure oscillations in large length-to-diameter two-phase micro-channel heat sinks, Int. J. Heat Mass Transf. 116 (2018) 273–291.

[6] S.G. Liter, M. Kaviany, Pool-boiling CHF enhancement by modulated porous-layer coating: theory and experiment, Int. J. Heat Mass Transf. 44 (2001) 4287–4311.

[7] G. Liang, I. Mudawar, Pool boiling critical heat flux (CHF) – part 2: assessment of models and correlations, Int. J. Heat Mass Transf. 117 (2018) 1368–1383.

[8] S. Toda, A study of mist cooling (1st report: investigation of mist cooling), Trans. JSME 38 (1972) 581–588.

[9] W.P. Klinzing, J.C. Rozzi, I. Mudawar, Film and transition boiling correlations for quenching of hot surfaces with water sprays, J. Heat. Treat. 9 (1992) 91–103.

[10] L. Lin, R. Ponnappan, Heat transfer characteristics of spray cooling in a closed loop, Int. J. Heat Mass Transf. 46 (2003) 3737–3746.

[11] M.E. Johns, I. Mudawar, An ultra-high power two-phase jet-impingement avionic clamshell module, J. Electron. Packag. 118 (1996) 264–270.

[12] S.N. Joshi, E.M. Dede, Two-phase jet impingement cooling for high heat flux wide band-gap devices using multi-scale porous surfaces, Appl. Therm. Eng. 110 (2017) 10–17.

[13] S. Mukherjee, I. Mudawar, Pumpless loop for narrow channel and micro-channel boiling from vertical surfaces, J. Electron. Packag. 125 (2003) 431–441.

[14] S. Lee, I. Mudawar, Investigation of flow boiling in large micro-channel heat exchangers in a refrigeration loop for space applications, Int. J. Heat Mass Transf. 97 (2016) 110–129.

[15] R. van Erp, R. Soleimanzadeh, L. Nela, G. Kampitsis, E. Matioli, Co-designing electronics with microfluidics for more sustainable cooling, Nature 585 (2020) 211–216.

[16] C.O. Gersey, I. Mudawar, Effects of heater length and orientation on the trigger mechanism for near-saturated flow boiling critical heat flux - II. Critical heat flux model, Int. J. Heat Mass Transf. 38 (1995) 643–654.

[17] J. Kim, J.S. Lee, Numerical study on the effects of inertia and wettability on subcooled flow boiling in microchannels, Appl. Therm. Eng. 152 (2019) 175–183.

[18] S. Hardt, F. Wondra, Evaporation model for interfacial flows based on a continuum-field representation of the source terms, J. Comput. Phys. 227 (2008) 5871–5895.

[19] J. Kim, J.Y. Cho, J.S. Lee, Flow boiling enhancement by bubble mobility on heterogeneous wetting surface in microchannel, Int. J. Heat Mass Transf. 153 (2020) 119631.

[20] W.H. Lee, A pressure iteration scheme for two-phase flow modeling multi-phase transport: fundamentals, Reactor Safety, Appl. 1 (1980) 407–431.

[21] W. Tang, J. Li, Z. Wu, J. Lu, K. Sheng, A numerical investigation of the thermal–hydraulic performance during subcooled flow boiling in MMCs with different manifolds, Appl. Therm. Eng. 236D (2024) 121820.

[22] Y. Huang, K. Chen, X. Tang, Y. Fang, Two-phase flow oscillation and distribution in parallel channels during R1233zd(E) subcooled flow boiling: a numerical study, Int. J. Heat Mass Transf. 218 (2024) 124778.

[23] J. Broughton, E. Torres, A. Narayanan, Y.K. Joshi, Experimental and numerical investigation of flow boiling in additive manufactured foam structures with vapor pathways, ASME. J. Heat Mass Transfer 146 (2) (2024) 021002.

[24] P. Cui, Z. Liu, H. Wu, Subcooled flow boiling in ultrahigh-aspect-ratio microchannels for high heat flux cooling, Int. Comm. Heat and Mass Transf. 151 (2024) 107221.

[25] Y. Guo, C. Zhu, L. Gong, Z. Zhang, Numerical simulation of flow boiling heat transfer in microchannel with surface roughness, Int. J. Heat Mass Transf. 204 (2023) 123830.

[26] I. Mudawar, S. Kim, J. Lee, A coupled level-set and volume-of-fluid (CLSVOF) method for prediction of microgravity flow boiling with low inlet subcooling on the international space station, Int. J. Heat Mass Transf. 217 (2023) 124644.

[27] Y. Sato, B. Niceno, Nucleate pool boiling simulations using the interface tracking method: boiling regime from discrete bubble to vapor mushroom region, Int. J. Heat Mass Transf. 105 (2017) 505–524.

[28] Y. Chen, K. Ling, H. Ding, Y. Wang, S. Jin, W. Tao, 3-D numerical study of subcooled flow boiling in a horizontal rectangular mini-channel by VOSET, Int. J. Heat Mass Transf. 183 (2022) 122218.

[29] Y. Chen, M. Ji, B. Gao, B. Wang, W. Li, K. Jiao, D. Sun, B. Yu, Effects of heterogeneous nucleation model on computational fluid dynamics simulation of flow boiling heat transfer in the mini-channel, Phys. Fluids 35 (2023) 123301.

[30] H. Alimoradi, M. Shams, N. Ashgriz, A. Bozorgnezhad, A novel scheme for simulating the effect of microstructure surface roughness on the heat transfer characteristics of subcooled flow boiling, Case Stud. Therm. Eng. 24 (2021) 100829.
[31] D. Mitrakos, A. Vouros, H. Bougioukou, G. Giustini, Computational fluid dynamics prediction of subcooled boiling of water using a mechanistic bubble-departure model, Nucl. Eng. Des. 412 (2023) 112465.
[32] L. Wang, J. Wang, Y. Li, CFD study on film boiling features of cryogenic fluid influenced by heat structures and gravity levels, Cryogenics 124 (2022) 103455.
[33] Y. Huo, C. Ma, J. Zhang, R. Zhang, R.G. Huang, Simulation study on thermal performance of two turns helium cryogenic oscillating heat pipe for superconducting accelerator, Radiat. Detect. Technol. Methods 7 (2023) 427–434.
[34] P. Xu, L. Chen, J. Chen, D. Mei, X. Zhang, X. Mi, J. Chen, Pressure drop characterization on cryogenic multiphase flow in spiral wounded heat exchanger under high mass flow conditions, Appl. Therm. Eng. 234 (2023) 121257.
[35] Y. Jiang, Y. Yu, Z. Wang, S. Zhang, J. Cao, CFD simulation of heat transfer and phase change characteristics of the cryogenic liquid hydrogen tank under microgravity conditions, Int. J. Hydrogen Energy 48 (2023) 7026–7037.
[36] W. Hong, Y. Wu, L. Hu, P. Miao, H. Liu, F. Liu, Y. Shi, Mixture modeling to simulate helium boiling: helium gas bubble trapped in high magnetic field, Phys. Fluids 35 (2023) 113303.
[37] J. Chen, R. Zeng, X. Zhang, L. Qiu, J. Xie, Numerical modeling of flow film boiling in cryogenic chilldown process using the AIAD framework, Int. J. Heat Mass Transf. 124 (2018) 269–278.
[38] Y. Zheng, H. Chang, Y. Qiu, C. Duan, J. Chen, H. Chen, S. Shu, Prediction of liquid hydrogen flow boiling critical heat flux condition under microgravity based on the wall heat flux partition model, Int. J. Hydrogen Energy 45 (2020) 7141–7150.
[39] D.A. Gubaidullin, B.A. Snigerev, Numerical simulation of heat transfer during boiling flow of cryogenic fluid in vertical tube, Lobachevskii J. Math. 41 (2020) 1210–1215.
[40] V. Ahuja, A. Hosangadi, T. Weathers, E. Baglietto, J. M. Pesich, M. Kassemi, Simulations of cryogenic line chilldown with advanced sub-grid wall boiling models, AIAA SCITECH 2024 Forum, AIAA 2024-0357, January 2024.
[41] S. Kim, N. Damle, I. Mudawar, J. Hartwig, Experimental heat transfer results and flow visualization of horizontal near-saturated liquid nitrogen flow boiling in uniformly heated circular tube under Earth gravity, Appl. Therm. Eng. 246 (2024) 122934.
[42] S. Kim, N. Damle, I. Mudawar, J. Hartwig, Cryogenic flow boiling in microgravity: effects of reduced gravity on two-phase fluid physics and heat transfer, Int. J. Heat Mass Transf. 218 (2024) 124751.
[43] S. Kim, D. Foster, N. Damle, I. Mudawar, J. Hartwig, Experimental investigation of flow orientation effects on cryogenic flow boiling, Int. J. Heat Mass Transf. 220 (2024) 124940.
[44] E.W. Lemmon, M.L. Huber, M.O. McLinden, NIST Standard Reference Database 23: Reference Fluid Thermodynamic and Transport Properties-REFPROP, Version 10.0, Gaithersburg, Maryland, 2018.
[45] J.U. Brackbill, D.B. Kothe, C. Zemach, A continuum method for modeling surface tension, J. Comput. Phys. 100 (1992) 335–354.
[46] M. Sussman, E.G. Puckett, A Coupled Level Set and Volume-of-Fluid method for computing 3D and axisymmetric incompressible two-phase flows, J. Comput. Phys. 162 (2000) 301–337.
[47] K.K. So, X.Y. Hu, N.A. Adams, Anti-diffusion method for interface steepening in two-phase incompressible flow, J. Comput. Phys. 230 (2011) 5155–5177.
[48] S. Kim, J. Lee, I. Mudawar, J. Hartwig, Computational investigation of vertical upflow boiling of liquid nitrogen and effects of bubble collision dispersion force, Int. J. Heat Mass Transf. 203 (2023) 123780.
[49] J. Lee, L. O'Neill, S. Lee, I. Mudawar, Experimental and computational investigation on two-phase flow and heat transfer of highly subcooled flow boiling in vertical upflow, Int. J. Heat Mass Transf. 136 (2019) 1199–1216.
[50] J.P. Lewis, J.H. Goodykoontz, J.F. Kline, Boiling heat transfer to liquid hydrogen and nitrogen in forced flow, NASA Technical Note D-1314 (1962).
[51] J. Lee, S. Kim, I. Mudawar, Assessment of computational method for highly subcooled flow boiling in a horizontal channel with one-sided heating and improvement of bubble dispersion, Int. J. Therm. Sci. 184 (2023) 107963.
[52] ANSYS FLUENT Theory Guide 15.0 , ANSYS Inc., Canonburg, PA, 2013.
[53] R. Mei, J.F. Klausner, Shear lift force on spherical bubbles, Int. J. Heat Fluid Flow 15 (1994) 62–65.
[54] S.L. Sharma, T. Hibiki, M. Ishii, C.S. Brooks, J.P. Schlegel, Y. Liu, J.R. Buchanan, Turbulence-induced bubble collision force modeling and validation in adiabatic two-phase flow using CFD, Nucl. Eng. Des. 312 (2017) 399–409.
[55] X. Li, W. Wei, R. Wang, Y. Shi, Numerical and experimental investigation of heat transfer on heating surface during subcooled boiling flow of liquid nitrogen, Int. J. Heat Mass Transf. 52 (2009) 1510–1516.
[56] Z. Liang, T. Biben, P. Keblinski, Molecular simulation of steady-state evaporation and condensation: validity of the Schrage relationships, Int. J. Heat Mass Trasnf. 114 (2017) 105–114.
[57] R.W. Schrage, A Theoretical Study of Interphase Mass Transfer, Columbia University Press, New York, 1953.
[58] I. Tanasawa, Advances in condensation heat transfer, in: J.P. Hartnett, T.F. Irvine (Eds.), Advances in Heat Transfer, Academic Press, San Diego, 1991.
[59] S. Levy, Forced convection subcooled boiling-prediction of vapor volumetric fraction, Int. J. Heat Mass Transf. 10 (1967) 951–965.
[60] S.M. Zivi, Estimation of steady-state steam void-fraction by means of the principle of minimum entropy production, J. Heat Transf. 86 (1964) 247–251.